https://doi.org/10.5194/egusphere-2026-6431
Preprint. Discussion started: 9 November 2026
© Author(s) 2026. CC BY 4.0 License.

Disentangling Atmospheric Turbulence from Hydrometeor Aerodynamics: Radar Spectrum Width Peaks and Microphysical Signatures within Dendritic Growth Zones

Sung-Ho Suh[1*]

Institutional addresses:

[1]Flight Safety Technology Division, NARO Space Center, Korea Aerospace Research Institute (KARI), 508 Haban-ro, Bongrae-myeon, Goheung-gun, Jeollanam-do, Republic of Korea

*Corresponding author: Dr. Sung-Ho Suh (*suhsh@kari.re.kr*)

Abstract

The Doppler velocity spectrum width (σ_v) observed by dual-polarization weather radar is widely used as a proxy for atmospheric turbulence, including convectively induced turbulence (CIT) hazardous to aviation. However, σ_v also responds to the aerodynamic behavior of frozen hydrometeors, so its interpretation within the dendritic growth zone (DGZ) remains ambiguous. This study combines a spheroidal aerodynamic response model with quasi-vertical profile (QVP) observations from eight precipitation cases recorded by the S-band dual-polarization radar at the Yongin testbed. Simulations show that particle geometry governs how efficiently a wind perturbation is converted into radial-velocity variance: the whole plane-crystal series, from plates to dendrites, responds far more strongly than columnar or rimed habits. A quantitative procedure identified a σ_v peak zone in five cases, all stratiform. In four of them σ_v showed no systematic relationship with vertical wind shear (*VWS*) but a temperature-dependent negative relationship with differential reflectivity (Z_{DR}); static stability and near-vertical radial-velocity observations argue against a thermally driven origin, while the ice-relative vapor density excess ($\Delta\rho_v$) maximum was positively related to, and vertically adjacent to, the σ_v maximum. Beneath the peak, an aggregation index derived from Z_H, Z_{DR}, and K_{DP} increased with σ_v magnitude, whereas a counterpart index for vapor-depositional growth did not. The cases separate into weak plate-dominated growth, strong dendritic growth, and one shear-driven peak unrelated to the DGZ. These results suggest that σ_v within growth layers is partly determined by the hydrometeors observed, so estimating turbulence inside precipitating systems requires knowledge of the microphysical state and hydrometeor type.

1. Introduction

The Doppler velocity spectrum width (σv) measured by weather radar quantifies the variance of scatterer velocities within a resolution volume and is routinely used to characterize atmospheric turbulence in precipitating systems (Hocking, 1985; Doviak and Zrnić, 1993; Melnikov and Doviak, 2009). Because turbulence is a leading contributor to CIT hazards, many studies have used σv to estimate the eddy dissipation rate (EDR) (Sharman et al., 2014; Kim et al., 2021). The measured σv is not, however, a turbulence quantity in itself: it aggregates turbulent motion, mean-wind shear across the sampling volume,

https://doi.org/10.5194/egusphere-2026-6431
Preprint. Discussion started: 9 November 2026
© Author(s) 2026. CC BY 4.0 License.

beam broadening, and the dispersion of hydrometeor fall velocities (Doviak and Zrnić, 1993). Retrievals model or remove the non-turbulent terms and attribute the residual to turbulence (Williams, 2012), so their reliability depends on whether every non-turbulent contribution has been accounted for.

That question takes a specific form within the DGZ (approximately -20 to -10℃), whose polarimetric structure is comparatively well documented. Descending through it, Z_H increases toward the ground while Z_{DR} reaches a local maximum near the level of most active dendritic growth and then decreases, and ρ_{hv} is reduced where crystal shapes are most diverse — interpreted as vapor-depositional growth followed by aggregation (Ryzhkov et al., 2016; Schrom and Kumjian, 2016; Griffin et al., 2018; Table 1). The behavior of σ_v in the same layer has received far less attention, and where an enhancement has been reported (Allabakash et al., 2019; Suh et al., 2023) its origin has not been resolved. Because the layer is conventionally located from the Z_{DR} maximum (Kennedy and Rutledge, 2011; Griffin et al., 2018), the inverse Z_{DR}–σ_v relationship reported by Suh et al. (2023) would imply that the two variables carry complementary rather than redundant information, and that a σ_v enhancement there need not indicate stronger turbulence.

Table 1. Summary of prior research on the principal features of dual-polarization radar variables within the DGZ. Arrows indicate the trend in each variable along the fall direction.

References	Z_H	Z_{DR}	K_{DP}	ρ_{hv}	V_R	σ_v
Ryzhkov et al. (2016)	↓	↑	.	↓	.	.
Schrom and Kumjian (2016)	↓	Max	.	.	↓	.
Griffin et al. (2018)	$\propto K_{DP}^{-1}$	Max	$\propto Z_{DR}^{-1}$	.	.	.
Allabakash et al. (2019)	↓	Max	↑	↓	.	↑
Suh et al. (2023)	↓	$\propto \sigma_v^{-1}$	.	↓	.	↑

A less examined contribution to σ_v is the aerodynamic diversity of the frozen hydrometeors themselves. Within the DGZ, ice-crystal habit changes rapidly with temperature and vapor supply (Pruppacher and Klett, 1997; Bailey and Hallett, 2009), producing forms spanning simple plates through highly branched dendrites (Libbrecht, 2005), and the vertical structure of the layer has been increasingly characterized by profiling observations (Von Terzi et al., 2022; Zhang et al., 2025). Planar, low-density habits experience irregular, tumbling fall motion, whereas compact or rimed particles fall more steadily.

This arises because planar crystals present a highly asymmetric cross-section to the airflow. Unlike compact or rimed particles, whose aerodynamic center of pressure remains close to their center of mass, planar habits have a large, irregular projected area relative to their mass, so small perturbations in orientation generate disproportionately large aerodynamic torques. As the particle rotates, its apparent cross-section and drag change continuously, producing a fluttering, non-monotonic descent (Willmarth et al., 1964; Field et al., 1997), as reproduced in simulations of freely falling ice crystals (Hashino et al., 2014; Nettesheim and Wang, 2018). Superimposed on a wind perturbation, this instability would amplify the along-beam velocity variance beyond what the same perturbation would produce for a compact particle, in which case σ_v peaks within the DGZ may reflect hydrometeor type as much as the magnitude of the disturbance, and CIT and EDR retrievals would misattribute microphysically amplified σ_v to stronger turbulence.

https://doi.org/10.5194/egusphere-2026-6431
Preprint. Discussion started: 9 November 2026
© Author(s) 2026. CC BY 4.0 License.

The study proceeds in four steps: a spheroidal aerodynamic response model simulates the sensitivity of σ_v to wind perturbation as a function of particle shape (Section 2); eight cases observed at YIT are analyzed using QVPs, and a quantitative procedure delimits the σ_v peak (Sections 3–4); σ_v is compared with independent indicators of atmospheric disturbance and with the accompanying thermodynamic and moisture conditions (Sections 5–6); and polarimetric diagnostics of aggregation are used to examine whether the microphysical evolution expected of planar crystals is observed above and below the peak (Section 7). Vertical wind shear (*VWS*) is adopted throughout as the observational index of atmospheric disturbance. Shear instability is the principal mechanism by which turbulence is generated in the free atmosphere, and shear-based quantities remain among the most skillful predictors in the diagnostics used operationally to forecast aviation turbulence and to estimate the eddy dissipation rate (Sharman and Pearson, 2017; Muñoz-Esparza et al., 2020).

The same quantity is used as the external forcing in the model of Section 2, so that the simulated and observed analyses address atmospheric disturbance in a single, consistent framework.

2. Theoretical Background: Aerodynamic Response of Frozen Hydrometeors

To evaluate how particle shape modulates the response of frozen hydrometeors to a wind perturbation — and hence the variance in V_R — a spheroidal aerodynamic response model was constructed. It does not reproduce a steady terminal fall speed but represents free fall under a prescribed particle orientation, resolving how a particle of given shape and density responds to an imposed perturbation, so the simulated quantity is comparable to the radial-velocity variance sampled by the radar. Each hydrometeor is an oblate or prolate spheroid whose habit-defining axes *a*, *b*, and *c* give its width, length, and height, oriented at a canting angle β relative to the vertical (Fig. 1). The habit fixes the particle's true shape, and the canting angle and the resulting apparent axis ratio γ may be regarded as further factors determining the cross-sectional area presented to the imposed flow; it is that area that governs how strongly the particle is displaced horizontally, so shape and orientation act together rather than either alone. The representation follows established relationships between hydrometeor density, axis ratio, and drag coefficient (Böhm, 1989; Hölzer and Sommerfeld, 2008; Loth, 2008). Surface irregularity enters through the surface-irregularity parameter ε_b prescribed for each plane-crystal habit in Table A1 (Kuroiwa et al., 1967); an irregular surface alters the effective area presented to the flow and so modifies the fall behavior itself (Böhm, 1989; Loth, 2008), which is why a more irregular particle can develop a larger spread of motion under the same forcing. The tumbling descent captured by this representation parallels studies of freely falling non-spherical bodies (Stringham et al., 1969; Suh et al., 2019).

https://doi.org/10.5194/egusphere-2026-6431
Preprint. Discussion started: 9 November 2026
© Author(s) 2026. CC BY 4.0 License.

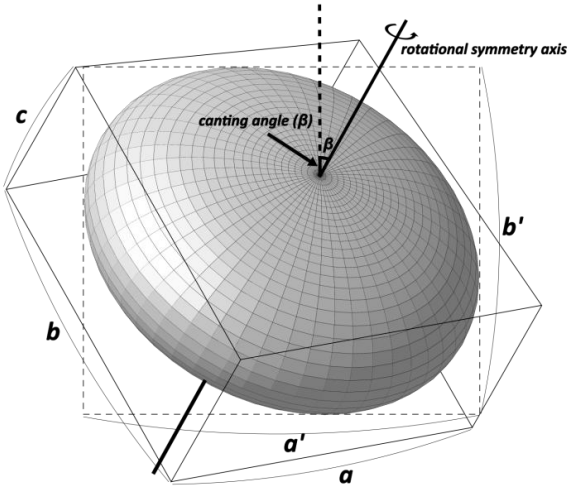


Figure 1. Schematic of the spheroidal hydrometeor model. The axes *a*, *b*, and *c* denote the particle's true width, length, and height (full dimensions, not radii); *a′* and *b′* denote the apparent width and length presented to the radar. The rotational symmetry axis and canting angle (*β*) are shown; the apparent axis ratio (*γ*) can differ from the true shape depending on *β*.

The particle's horizontal response to an imposed crosswind acceleration (*α*, 10–60 m s^{-2}) is combined with its free-fall motion under the prescribed orientation and projected onto the radar beam to give the V_R the radar would sample; bulk density was held constant, so the resulting spread in V_R is attributable to shape and orientation. At fixed *α* (Fig. 2a) each *γ* traces its own curve as *β* sweeps through 0–60°, with near-spherical particles confined to small C_{DV} and low V_R; increasing *α* at fixed *β* (Fig. 2b) translates the family toward larger V_R while preserving their ordering in *γ*. C_{DV} rose sharply once V_R exceeded roughly 7–8 m s^{-1}, and the canting-induced spread dV_R grew approximately linearly with *α*, the largest sensitivity occurring at the most extreme axis ratios (Fig. 2c–d). It therefore measures how efficiently a shape converts a perturbation into radial-velocity variance — not controlled by *α* alone, since particle mass and axis ratio enter the same drag relationship.

https://doi.org/10.5194/egusphere-2026-6431
Preprint. Discussion started: 9 November 2026
© Author(s) 2026. CC BY 4.0 License.

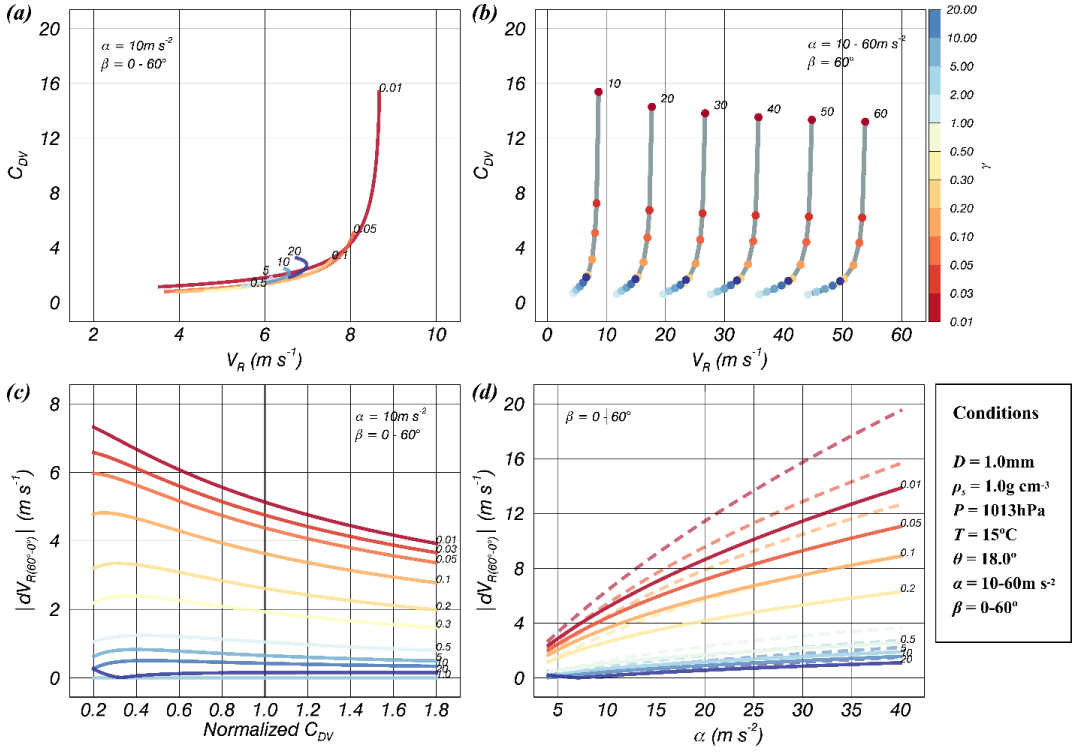


Figure 2. Simulated relationships between V_R and the crosswind drag coefficient (C_{DV}) at an elevation angle of 0°, for (a) α = 10 m s^{-2} with β = 0–60° and (b) α = 10–60 m s^{-2} with β = 60°. Colors denote the apparent axis ratio γ, scaled to the right of (b). (c) Dependence of the canting-induced V_R spread on normalized C_{DV}. (d) dV_R versus α under the conditions in the inset; solid and dashed lines denote normalized C_{DV} = 1 and 0.5.

The physical properties in Table A1 were then used to simulate eight representative habits (P1a–P3b: the plate-to-dendrite series; R4b: a rimed particle; C1a and C3a: needle and columnar types) under conditions approximating natural stratiform snowfall. Aerodynamic coefficients for the plane-crystal group follow Nettesheim and Wang (2018) as summarized in Table A2, and the particle population at each acceleration was drawn from an exponential size distribution (Sekhon and Srivastava, 1970) over the size range prescribed separately for each habit in Table A1, following the observed dimensions of natural crystals (Auer and Veal, 1970); details are given in the Appendix.

The response separates by particle geometry (Fig. 3). The plane-crystal series produced a large σ_v response, rising from the simple plate through the sector and stellar habits to the dendrite (P3b), which reached 2–3 m s^{-1} at the higher accelerations, whereas the columnar and needle habits remained below about 0.3 m s^{-1} and the rimed particle behaved similarly. Two features matter. First, particle shape is also found to be a factor determining the amplitude of the response: at fixed forcing σ_v increases monotonically with the planarity and geometric complexity of the habit, so shape and forcing together, rather than forcing alone, set the amplitude. Second, the property that appears to govern this is the planar geometry shared across the whole plate-to-dendrite series rather than anything unique to dendrites: the dendrite is the endpoint of a continuum, and even the simple plate responds several times more strongly than a columnar crystal of comparable mass. The simulated magnitudes exceed the observed peaks because the imposed accelerations span the full sensitivity envelope of the model; the relevant result is the relative ranking.

https://doi.org/10.5194/egusphere-2026-6431
Preprint. Discussion started: 9 November 2026
© Author(s) 2026. CC BY 4.0 License.

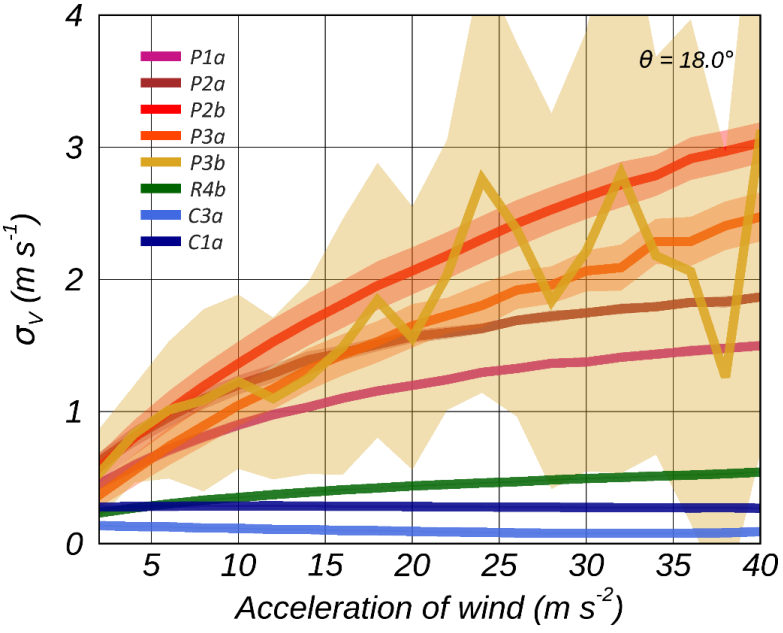


Figure 3. Simulated σ_v as a function of wind acceleration for eight hydrometeor habits at an elevation angle of θ = 18.0°. Colored lines and shaded envelopes denote the ensemble mean and ±1 standard deviation (STD) for each habit (see Table A1).

3. Radar Observations, Analysis Cases, and Processing Strategy

3.1. Radar system and precipitation cases

This study used the S-band (2.88 GHz) dual-polarization weather radar operated at YIT by the Weather Radar Center of the Korea Meteorological Administration (KMA) since July 2014 (Table 2). YIT lies in Yongin city near the Seoul metropolitan area and provides an effective observation range of up to 240 km; a co-located automatic weather station (AWS) and upper-air sounding site (RS) provide independent surface and profile measurements (Fig. 4).

Table 2. Specifications of Yongin Testbed dual-pol weather radar (YIT).

Specifications	Details
Model	DWSR-8501 S/K-SDP
Manufacturer	EEC (US)
Transmitting tube	Klystron
Antenna diameter	8.5 m
Transmission frequency	2.88 GHz
Peak power	850 KW
Effective observation range	240 km
Beam / Pulse width	0.94° / 2 μs
Wavelength	10.41 cm

https://doi.org/10.5194/egusphere-2026-6431
Preprint. Discussion started: 9 November 2026
© Author(s) 2026. CC BY 4.0 License.

Range gate size	250 m
Elev. height	473 m
Long. / Lat.	127.2852 °E / 37.2063 °N
Obs. interval	10 min

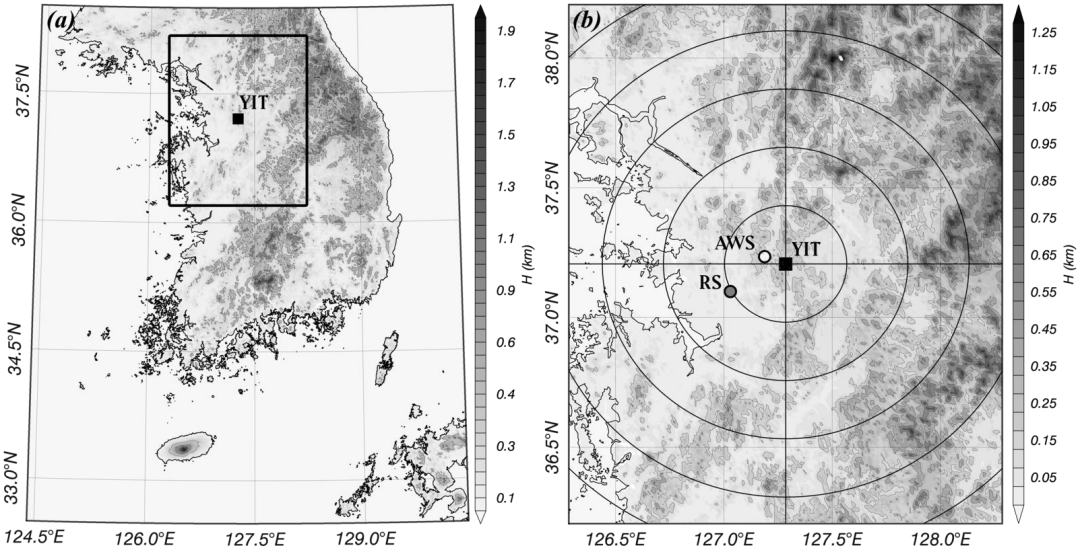


Figure 4. (a) Location of the YIT radar (black square) and its analysis domain (box) within the Republic of Korea, shaded by terrain height. (b) Detailed view of the YIT radar site with the co-located AWS (open circle) and radiosonde site (RS, filled circle); range rings are drawn at 25 km intervals.

The polarimetric variables follow standard dual-polarization practice (Doviak and Zrnić, 1993). Z_H (dBZ) responds to hydrometeor size and number concentration; Z_{DR} (dB) is a proxy for particle shape and orientation; K_{DP} (° km^{-1}) is sensitive to the concentration and anisotropy of oriented non-spherical particles; and ρ_{hv} measures the diversity of shapes, sizes, and orientations within the resolution volume. Together with σ_v and V_R, these allow particle shape and fall behavior to be inferred jointly — the basis for separating the microphysical and turbulent contributions to σ_v in Sections 5–7, an approach applied previously to winter precipitation at other S-band systems (Kennedy and Rutledge, 2011).

Eight precipitation cases observed between 2015 and 2016 were selected, spanning stratiform events with a well-developed bright band and convective events retained for contrast (Fig. 5). These cases, hereafter SW1–SW4, CP5, CP6, SP7, and CS8, form the basis of the QVP analysis that follows.

Case selection and precipitation-type classification were treated as separate steps. Precipitation type was classified from the composite maximum reflectivity at the lowest elevation angle over the analysis period (Fig. 5): cases in which this maximum did not exceed Z_H = 40 dBZ were classified as stratiform, the remainder as convective (Chen et al., 2022). Separately, and as a selection criterion applied before that classification, strongly convective systems reaching Z_H > 50 dBZ were excluded altogether, since vigorous internal turbulence would dominate σ_v. Cases were further retained only where echoes with Z_H > 5 dBZ persisted for at least 3 hours and spanned a depth exceeding 2 km, ensuring a stable QVP. Eight cases satisfied these criteria (Table 3); labels encode type and season, the first letter denoting stratiform (S) or convective (C), the second winter (W), spring (P), or summer (S).

https://doi.org/10.5194/egusphere-2026-6431
Preprint. Discussion started: 9 November 2026
© Author(s) 2026. CC BY 4.0 License.

Table 3. Information of precipitation cases selected in this study. Ground temperature was obtained from the AWS (37.2345°N, 127.1883°E) located approximately 9.1 km away from YIT.

Case	θ for QVP	Ground T (°C)	Date	Time (LST)		Type	Season
				YIT	RS		
SW1	16.4	-2.7 – -1.3	16. Feb. 2015	05-07	06	Stratiform	Winter
SW2	16.4	3.2 – 3.8	21. Feb. 2015	12-14	12	Stratiform	Winter
SW3	19.0	1.3 – 2.8	27. Feb. 2016	01-04	03	Stratiform	Winter
SW4	19.0	3.9 – 6.1	28. Feb. 2016	12-14	12	Stratiform	Winter
CP5	17.3	18.9 – 21.9	02. May. 2016	19-21	18	Convective	Spring
CP6	17.3	14.4 – 15.1	10. May. 2016	09-12	09	Convective	Spring
SP7	17.3	17.4 – 21.9	24. May. 2016	01-06	03	Stratiform	Spring
CS8	17.3	23.4 – 24.0	01. Jul. 2016	19-21	21	Convective	Summer

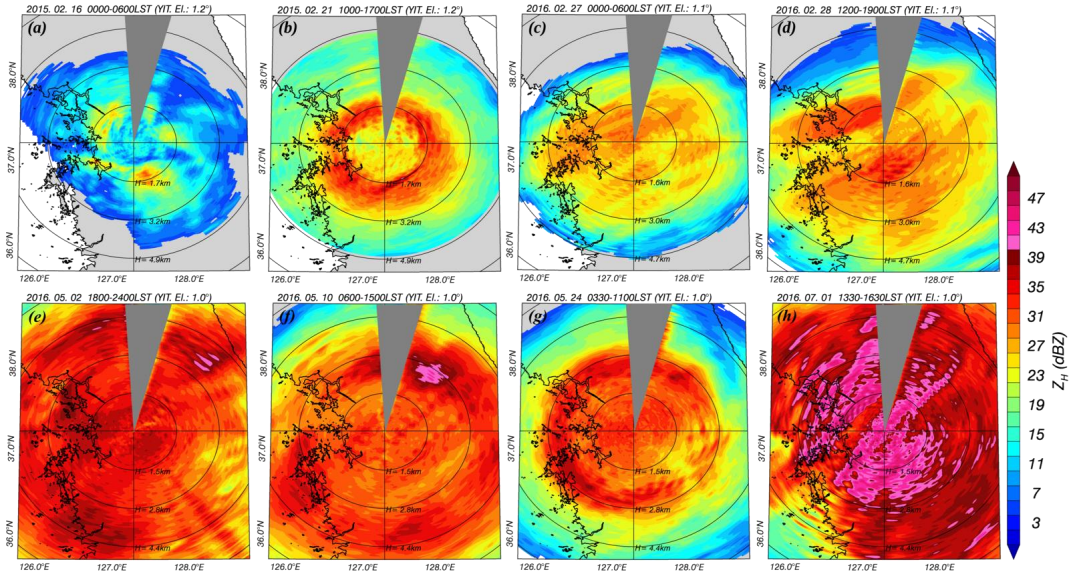


Figure 5. Composite maximum Z_H in PPI at the lowest elevation angle for the eight analysis cases (a–h), with the corresponding observation period and elevation angle indicated above each panel. The gray-shaded region in each panel denotes the beam-blockage area at the lowest elevation angle.

3.2. Analysis strategy and data quality control

The QVP is an efficient scheme generated from a single radar sweep; through azimuthal averaging its variables are particularly effective for resolving the microphysical features of frozen hydrometeors (Ryzhkov et al., 2016). Because YIT is a non-operational, research-oriented system whose scan strategy is adjusted to the observation purpose, the elevation angle (θ) used to generate the QVPs was selected case by

https://doi.org/10.5194/egusphere-2026-6431
Preprint. Discussion started: 9 November 2026
© Author(s) 2026. CC BY 4.0 License.

case within 16.4–19.0° (Table 3). At the maximum analysis height of H = 12 km the corresponding slant ranges are approximately 42.55, 40.40, and 36.81 km, neglecting Earth curvature.

The radar data were processed through a series of quality-control steps. A fuzzy-logic algorithm removed non-meteorological targets (Gourley et al., 2007); because σ_v exhibits large variance at low signal-to-noise ratio (SNR), measurements with SNR < 20 dB were discarded (Zhang et al., 2009), and only returns with $Z_H \geq 5$ dBZ were retained. K_{DP} was derived from the differential phase rather than used as supplied: gates with $\rho_{hv} < 0.6$ or with range-wise non-monotonic Φ_{DP} were discarded, the remaining profile was smoothed along range over a 2 km window, and K_{DP} was obtained as half its range derivative. In constructing the QVPs, all variables at a range bin were discarded if fewer than 20% of the azimuths there satisfied $Z_H > 5$ dBZ.

Because the projected area of a target — and therefore its measured differential reflectivity — depends on the line-of-sight direction, Z_{DR} was calibrated to its equivalent horizontal-viewing value. This step is essential here because the elevation angle differs between cases, and the case-to-case Z_{DR} comparisons in Sections 5 and 7 would otherwise be ambiguous. The elevation-angle dependence follows Ryzhkov et al. (2005):

$$ZDR(\theta) = \frac{ZDR(0°)}{[ZDR(0°)^{1/2} sin^2\theta + cos^2\theta]^2} \quad \text{(Eq. 1)}$$

where Z_{DR} is expressed on a linear scale. For the elevation angles used here the correction yields $Z_{DR}(0°) = 0.916^{-1}Z_{DR}(16.4°)$, $0.906^{-1}Z_{DR}(17.3°)$, and $0.887^{-1}Z_{DR}(19.0°)$. It is applied to every Z_{DR} value from the QVP elevations reported below. It is not applied to the near-vertical (θ = 80°) scans of Section 6, at which Eq. 1 converges toward 0 dB irrespective of particle shape and therefore cannot be inverted.

The environmental variables were drawn from two sources. Horizontal wind, and hence *VWS*, was taken from the Osan radiosonde soundings, provided by the Republic of Korea Air Force at 6- or 12-hourly intervals. Temperature and humidity — and therefore $\Delta\rho_v$, potential temperature, and equivalent potential temperature — were taken from the Japan Meteorological Agency Meso-Scale Model (MSM) reanalysis, on a 5 km grid with 16 pressure levels between 1000 and 100 hPa. Radiosonde humidity is subject to a temperature-dependent dry bias and to a response lag that grows as temperature falls, and the corrections for these errors are instrument-specific (Miloshevich et al., 2004; Moradi et al., 2013); the moisture fields were therefore taken from the model analysis. MSM fields were extracted at the radar observation time, whereas the soundings are fixed to synoptic hours, so that in some cases a difference of up to a few hours remains.

Because both sources are reported on coarser vertical grids than the radar, the environmental variables were resampled onto the QVP gate altitudes, spaced by roughly 70–80 m. Temperature and humidity are continuous scalar fields, so reconstructing their profiles with a smooth function is justified, and a smoothing cubic spline with the smoothing parameter selected by generalized cross-validation was used, which also keeps the gradients evaluated in Section 6 continuously differentiable. *VWS*, a non-negative quantity already obtained by differentiation, was treated differently: trial application of the same spline underestimated sharp shear maxima and overshot to negative values near zero, so *VWS* was computed on the native sounding levels, whose vertical spacing is approximately 0.3 km. The effective vertical resolution of the thermodynamic fields remains that of the MSM grid, about 1.5 km within the DGZ, so vertical separations quoted at finer scales are used comparatively between cases.

3.3. Identification of the σ_v peak zone

The σ_v enhancement examined here is not coincident with the DGZ as a whole but is a localized feature developing within it, whose altitude and depth vary from case to case. Suh et al. (2023) identified an

https://doi.org/10.5194/egusphere-2026-6431
Preprint. Discussion started: 9 November 2026
© Author(s) 2026. CC BY 4.0 License.

enhanced-spectrum-width layer associated with solid hydrometeor growth but did not delimit it quantitatively; a quantitative procedure is therefore introduced here. Profiles of median σ_v and its vertical gradient over the full analysis period (> 1 hr) were smoothed over a ±1-gate window, and for each local extremum only the point holding the largest gradient magnitude within a ±2-gate neighborhood was retained as a candidate boundary; values below the melting layer (Fig. 7) were excluded. The altitude of the σ_v maximum (H_σ) defines the core, and the nearest candidate extrema bracketing it define the boundaries, each extended by ±2 vertical windows, corresponding to approximately ±0.16 km at YIT, to allow for computational uncertainty. A candidate zone thicker than 1.5 km was rejected as implausible, exceeding the depth spanned by −20 to −10°C under a lapse rate of 6.5°C km^{-1} (Wallace and Hobbs, 2006). The resulting layer, termed the σ_v peak zone, lies within — and is generally much shallower than — the DGZ.

4. Vertical Structure of the σ_v Peak

Applying this procedure isolates a well-defined σ_v peak zone in five of the eight cases; no coherent peak was found in CP5, CP6, or CS8. The five are those classified as stratiform (SW1–SW4 and SP7; Table 3), which suggests the feature is characteristic of stratiform ice-phase precipitation. Expressed in temperature, the peaks fall into distinct groups: SW1 and SW2 near −10°C, SW3 and SW4 between about −15 and −20°C, and SP7 lowest of all, between roughly −5 and −10°C (Fig. 6). In SW3 and SW4 the radar did not resolve a clear upper boundary, and the peak zone was truncated at the top of the analysis domain.

https://doi.org/10.5194/egusphere-2026-6431
Preprint. Discussion started: 9 November 2026
© Author(s) 2026. CC BY 4.0 License.

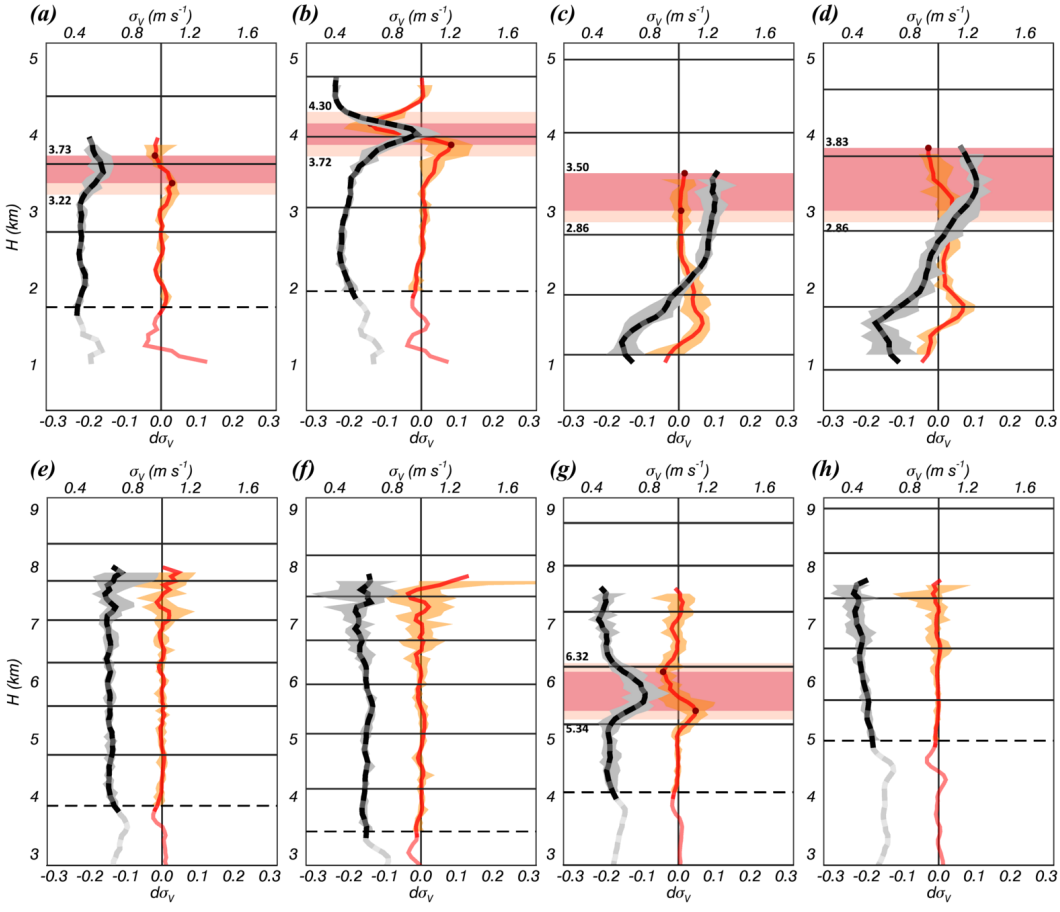


Figure 6. Vertical profiles of σ_v (black) and its vertical gradient $d\sigma_v$ (orange) for the eight cases, (a) SW1, (b) SW2, (c) SW3, (d) SW4, (e) CP5, (f) CP6, (g) SP7, and (h) CS8, used to determine the σ_v peak zone (shaded band). Red circles mark the extrema of $d\sigma_v$ retained as boundary candidates, and the numbers give the top and bottom altitudes (km). The dashed line marks the melting layer, and the solid lines are isotherms at 5°C intervals, from −5°C at the lowest solid line in each panel to progressively colder values upward.

Figure 7 shows what the other radar variables are doing where the σ_v peak occurs. In every case Z_H decreases with height as expected above the bright band, and ρ_{hv} is depressed through the middle troposphere. Against this background the σ_v peak zone is consistently co-located with, or immediately adjacent to, a local Z_{DR} enhancement and a local ρ_{hv} minimum — normally taken to indicate pristine, highly aspherical crystals (Schrom and Kumjian, 2016). The polarimetric variables vary appreciably across the σ_v peak in every case, and most markedly in SW3 and SW4, where the departures of Z_{DR}, K_{DP}, and ρ_{hv} from the surrounding profile are the largest of the data set. The four winter cases show this alignment most clearly; SP7 does not, its peak lying distinctly below the Z_{DR} maximum.

https://doi.org/10.5194/egusphere-2026-6431
Preprint. Discussion started: 9 November 2026
© Author(s) 2026. CC BY 4.0 License.

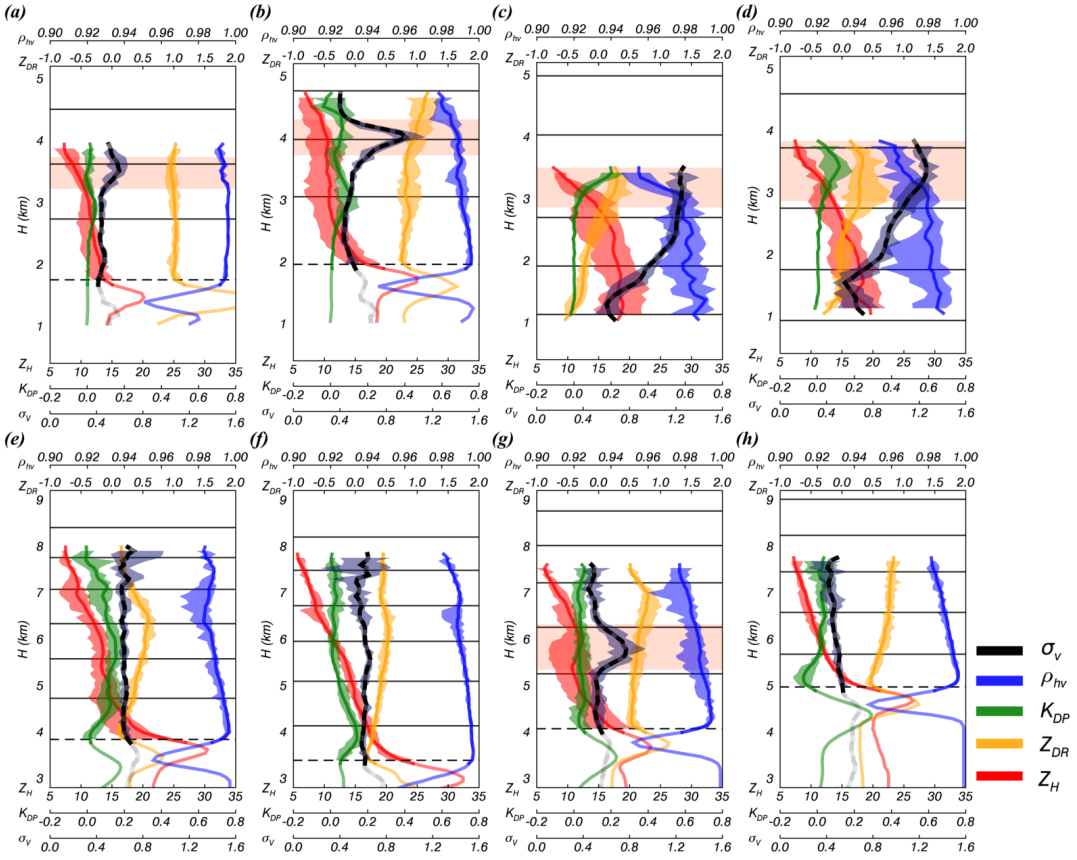


Figure 7. Average QVP of Z_H, Z_{DR}, K_{DP}, and ρ_{hv} (colored lines with shaded ±1 STD envelopes), and σ_v (black), for the eight analysis cases (panels as in Fig. 6). The dashed line marks the melting layer; the solid lines are isotherms at 5°C intervals, as in Fig. 6, and the shaded band marks the σ_v peak zone determined in Section 3.3 (Fig. 6).

5. Relationship between σ_v and Atmospheric Disturbance

The analysis is restricted to $-20 < T < -3$°C: the upper bound follows the conventional top of the DGZ and also reflects a practical limit, since in several cases the radar did not resolve colder levels, and the lower bound keeps the analysis clear of the melting layer. This domain is divided into four contiguous, non-overlapping bands — the top of the DGZ (−20 to −17°C), the center (−17 to −13°C), the bottom (−13 to −8°C), and a below-DGZ reference band (−8 to −3°C). The center spans the temperatures over which dendritic habits are most actively generated. The bottom band was extended to −8°C so as to capture as much as possible of the microphysical evolution of particles originating from the dendritic layer; for the same reason the reference band begins at −8°C, as far as practicable from DGZ-related processes while remaining clear of the melting layer.

The soundings show the background conditions of each case (Fig. 8). The sounding site lies within the horizontal domain sampled by the QVPs, and the balloon drifts further into that domain as it ascends. The site lies in the midlatitude westerlies and every case propagated from west to east, so the soundings sample the same air mass that the QVPs average over, though not the identical volume at the identical instant. Wind speed generally increased with height, though not monotonically in SW2, CP5, and CS8.

https://doi.org/10.5194/egusphere-2026-6431
Preprint. Discussion started: 9 November 2026
© Author(s) 2026. CC BY 4.0 License.

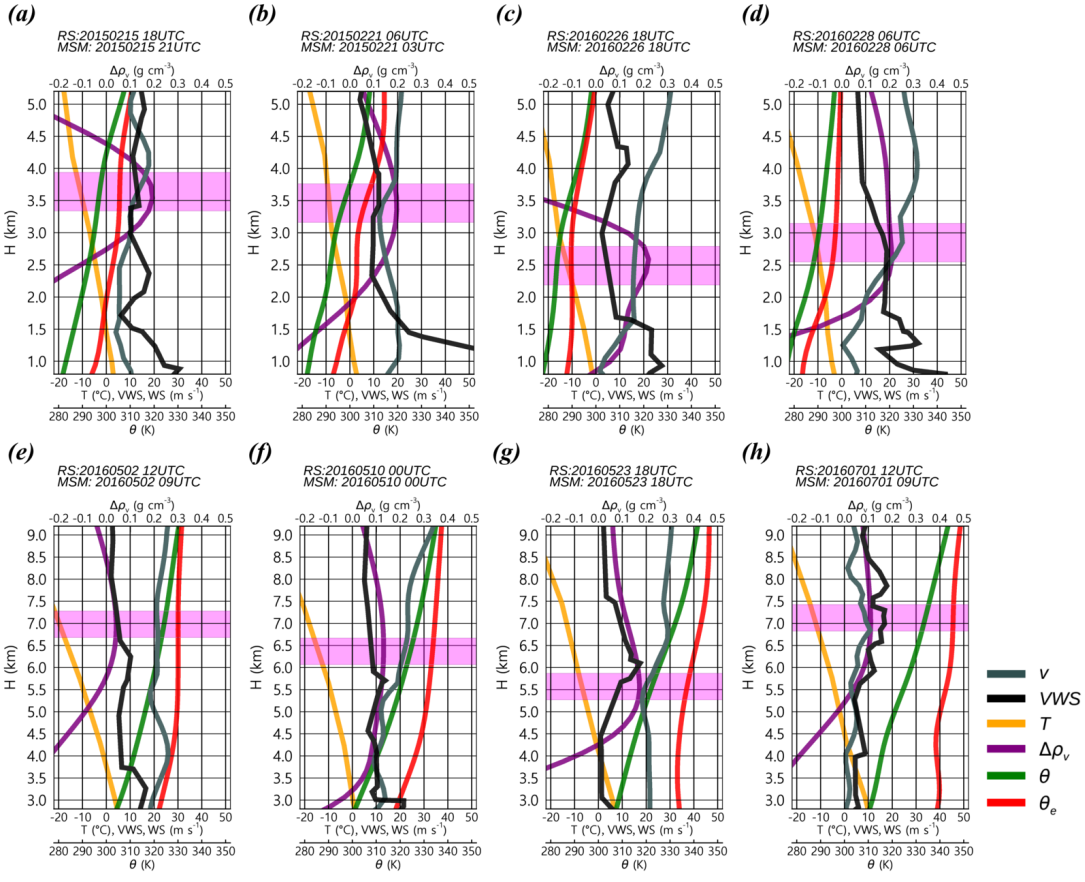


Figure 8. Vertical profiles of the environmental variables. Horizontal wind speed (v, gray) and *VWS* (black) are from the Osan radiosonde soundings; temperature (T, orange), $\Delta\rho_v$ (purple), potential temperature (θ, green), and equivalent potential temperature (θ_e, red) are from the JMA MSM analysis. Observation times of each source are given above every panel (RS, radiosonde; MSM, model analysis). Shaded bands mark where $\Delta\rho_v$ lies within the highest 10% of the profile.

If the σ_v peak were primarily turbulence-driven, σ_v should increase with *VWS*. Averaged over the peak zone it does not: cases occupy a narrow band of elevated σ_v (0.4–1.3 m s^{-1}) across a wide range of *VWS* (0–30 m s^{-1} km^{-1}), with no systematic increase (Fig. 9a). The contrast with the below-DGZ band is instructive: within $-8 < T < -3$℃ the two do increase together as expected for shear-generated variance, so it is within the DGZ that the relationship weakens. Restricting the comparison to the center of the DGZ sharpens this: SW3 and SW4 show the largest σ_v under some of the weakest *VWS*, while SW1, SW2, and CP6, with comparable or stronger *VWS*, show substantially smaller σ_v (Fig. 9b). SP7 behaves differently: within the center of the DGZ its *VWS* is among the weakest of all cases, yet within its own peak zone the *VWS* interquartile range becomes the largest of any case (Fig. 9c), and the sounding maximum of *VWS*, about 20 m s^{-1} km^{-1}, occurs near 6 km, coinciding with the altitude of its σ_v peak (Fig. 8g).

https://doi.org/10.5194/egusphere-2026-6431
Preprint. Discussion started: 9 November 2026
© Author(s) 2026. CC BY 4.0 License.

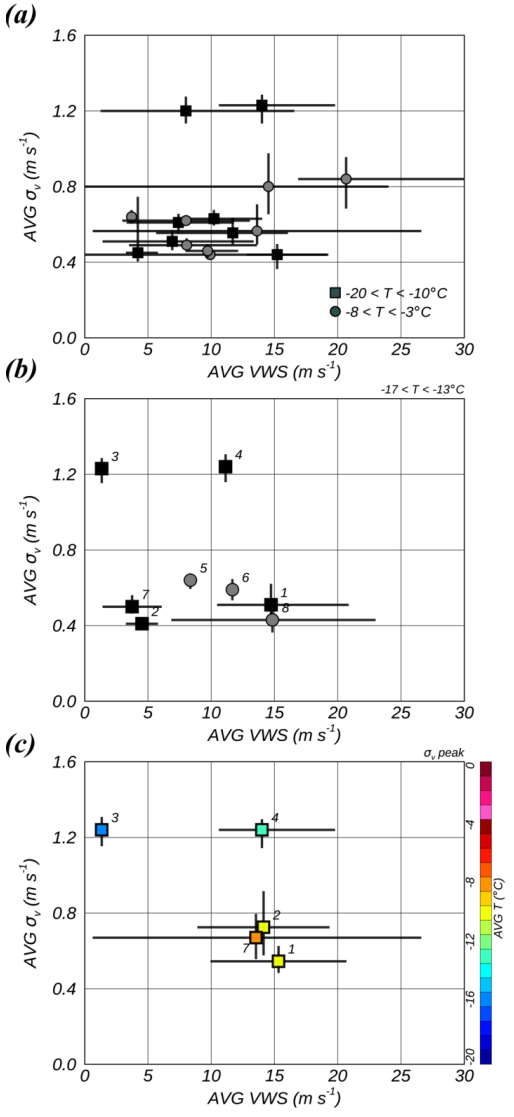


Figure 9. Case-averaged σ_v versus *VWS*; the solid line denotes the interquartile range. (a) Values for the DGZ σ_v peak zone (black squares, cases with an identified peak) and for the below-DGZ reference band (−8 to −3°C, gray circles, cases without one). (b) As in (a), restricted to the center of the DGZ, with case numbers labeled. (c) As in (b), but for the σ_v peak zone, colored by case-averaged temperature.

Because *VWS* alone does not account for the peaks, the co-variability of σ_v with Z_{DR} — a proxy for apparent particle shape — was examined next. Over the full domain the two are anti-correlated: as Z_{DR} falls toward 0 dB, σ_v rises toward 1.2–1.3 m s^{-1} while ρ_{hv} decreases simultaneously (Fig. 10a). This has a physical reading that does not require assuming a habit: increasing orientation disturbance drives the time-averaged apparent shape toward sphericity, lowering Z_{DR}, while widening the spread of apparent shapes within the resolution volume, lowering ρ_{hv}. Fitting the relationship shows the slope steepening toward colder temperatures, most negative near −15 to −20°C (Fig. 10b), and restricting the comparison to the peak zone

https://doi.org/10.5194/egusphere-2026-6431
Preprint. Discussion started: 9 November 2026
© Author(s) 2026. CC BY 4.0 License.

reproduces this at case level (Fig. 10c). Williams et al. (2013) compared NEXRAD Z_{DR} in winter storms with coincident airborne probe measurements and found the observations consistent with populations of hexagonal flat-plate crystals, supporting this reading.

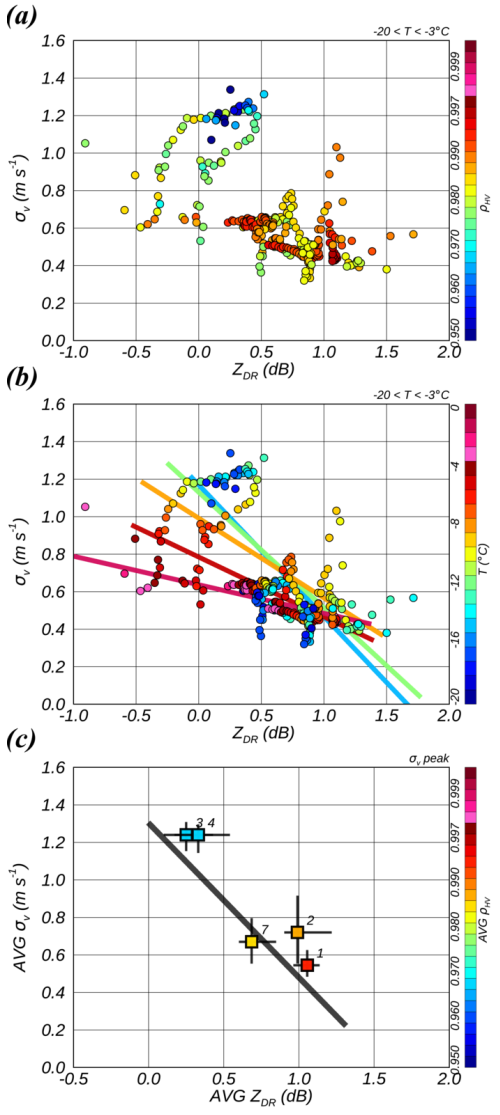


Figure 10. (a) σ_v versus Z_{DR} for $-20 < T < -3$°C, colored by ρ_{hv}. (b) As in (a), colored by temperature, with linear regressions fitted within 3°C-wide temperature bands. (c) Case-averaged σ_v versus Z_{DR} for the σ_v peak zone in each case, colored by average ρ_{hv}, with the overall linear regression shown.

6. Thermodynamic and Moisture Characteristics near the σ_v Peak

Two further explanations for the σ_v peak were examined. The first, latent-heat release producing local instability and buoyant updrafts, would act independently of particle shape and would therefore compete

https://doi.org/10.5194/egusphere-2026-6431
Preprint. Discussion started: 9 November 2026
© Author(s) 2026. CC BY 4.0 License.

with the aerodynamic interpretation; the second, the moisture conditions that determine which habits form, would instead support it. The first was tested using the vertical gradients of potential and equivalent potential temperature, which measure static stability (Wallace and Hobbs, 2006). Figure 11a compares the domain-averaged $d\theta_e/dz$ (gray) with the value confined to the σ_v peak zone (black); CP5, CP6, and CS8 are omitted, no peak having been identified there. Of the five remaining cases the peak-zone value exceeds the domain mean in SW2, SW3, and SP7 and falls below it in SW1 and SW4. Figure 11b shows the difference between the peak-zone value and that over reference layers of twice and three times the peak depth; its sign agrees with Fig. 11a in all cases and its magnitude increases as the reference layer widens.

This runs counter to what buoyant destabilization would require. If latent heating within the peak were generating the σ_v enhancement, the peak layer would be expected to be less stable than its surroundings in every case; instead three of the five are more stable, and SW3 — with one of the strongest peaks — is among them. Latent-heat-driven buoyancy therefore does not appear to be a general explanation for the feature.

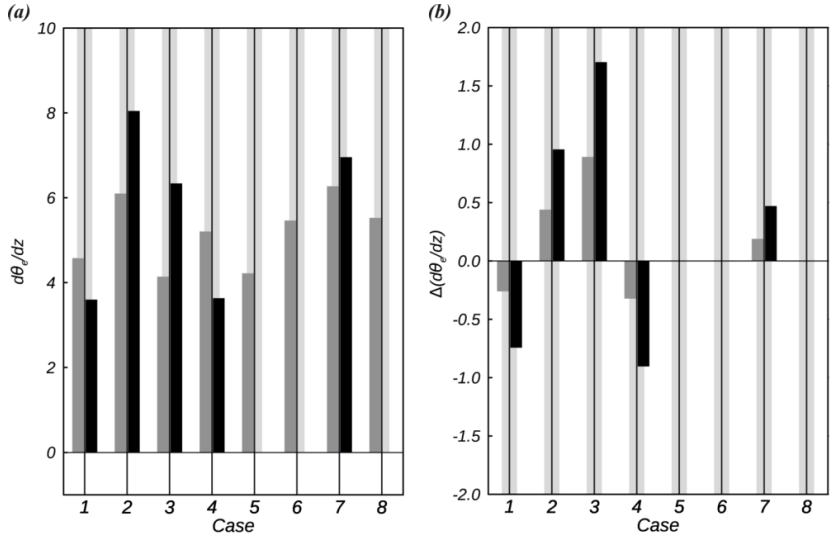


Figure 11. (a) Height-dependent equivalent-potential-temperature gradient ($d\theta e/dz$) averaged over −20 to −3°C domain (gray) and over the σ_v peak zone specifically (black), for the eight analysis cases. (b) Difference between $d\theta e/dz$ within the σ_v peak zone and $d\theta e/dz$ computed over reference layers of twice (gray) and three times (black) the σ_v peak depth, both centered on the σ_v peak — i.e., $\Delta(d\theta e/dz)$ = ($d\theta e/dz$)peak − ($d\theta e/dz$)reference.

A second line of evidence comes from near-vertical (θ = 80°) QVPs. Because YIT is a research radar whose scan strategy is revised periodically, such scans are not available throughout; among the cases with a resolved peak they were performed only for SW3 and SW4, which is why the following analysis is limited to those two. At this elevation the radial velocity is dominated by its vertical component (sin 80° ≈ 0.98), so V_R closely approximates the hydrometeor fall velocity (Atlas et al., 1973; Ryzhkov et al., 2016), and a thermally driven updraft would be expected to appear as a reduced or reversed downward V_R. Neither case shows such a signature: V_R instead becomes increasingly negative through the peak, whereas σ_v remains nearly constant (SW3) or decreases slightly (SW4) (Fig. 12). That σ_v does not broaden through the peak suggests that hydrometeors with markedly different fall speeds, such as dendrites and their aggregates (Locatelli and Hobbs, 1974; Heymsfield and Westbrook, 2010), are not mixed there. Under idealized conditions, with the near-vertical V_R as a proxy for the terminal velocity, the standard deviation of hydrometeor terminal velocities, σ_{Vt}, is at most about 0.4 m s^{-1} (Fig. 12). Its projection onto the beam, σ_{Vt}

https://doi.org/10.5194/egusphere-2026-6431
Preprint. Discussion started: 9 November 2026
© Author(s) 2026. CC BY 4.0 License.

sinθ, corresponds to the terminal-velocity term of the spectrum width (Doviak and Zrnić, 1993), and its contribution to σ_v^2 in the peak zone at $\theta = 19°$ is about 1 % ($\sigma_{Vt}^2 \sin^2\theta / \sigma_v^2 \approx 0.4^2 \times \sin^2 19° / 1.2^2 \approx 0.012$).

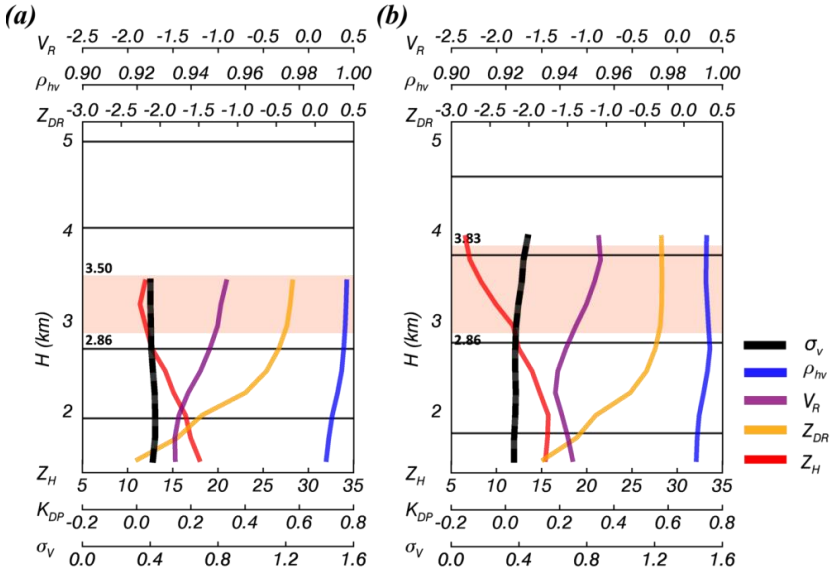


Figure 12. Average near-vertical ($\theta = 80°$) QVP of Z_H, Z_{DR}, ρ_{hv}, σ_v, and radial velocity (V_R) for (a) SW3 and (b) SW4; K_{DP} is unavailable at this elevation. The shaded band marks the σ_v peak zone determined in Section 3.3, with its top and bottom altitudes (km), and the solid horizontal lines are isotherms as in Fig. 6.

The moisture pathway was examined next. $\Delta\rho_v$ exceeded the 0.2 g m^{-3} threshold associated with branched, dendritic growth (St-Pierre and Thériault, 2015) only in SW3 and SW4; in SW1 and SW2 it reached values very close to 0.2 g m^{-3}. Comparing the magnitude and altitude of the $\Delta\rho_v$ maximum with those of the σ_v maximum reveals three features (Fig. 13). The two maxima are positively related over the full domain (Fig. 13a); their vertical separation is small in cases with an identified peak, generally within 0.5 km, and larger in cases without one; and restricting the comparison to the center of the DGZ preserves the positive relationship but loses the largest $\Delta\rho_v$ values (Fig. 13b), whereas restricting it to the peak zone recovers a distribution resembling the full domain (Fig. 13c). The largest vapor excess therefore appears more closely related to the σ_v peak than to a fixed temperature, and *VWS* shows no corresponding organization.

The habit-temperature relationship helps explain why the peaks are distributed as they are. Dendritic growth is not confined to −15°C but proceeds over roughly −12 to −17°C, while plate-like habits form over a broader and warmer range extending to about −8°C (Pruppacher and Klett, 1997). The peaks of SW1 and SW2, near −10°C, therefore lie where plates are favored and dendrites are possible only at the warm edge of their range, which is consistent with their $\Delta\rho_v$ approaching but not exceeding the dendritic threshold and with the more modest peaks they produce. SW3 and SW4, peaking between about −15 and −20°C, lie within the range over which dendritic growth is most vigorous, and it is in these two cases that $\Delta\rho_v$ exceeds the threshold. The temperature at which a σ_v peak appears is thus not incidental: it selects which habit can dominate the layer, and through that, how strongly the population responds to a given perturbation.

https://doi.org/10.5194/egusphere-2026-6431
Preprint. Discussion started: 9 November 2026
© Author(s) 2026. CC BY 4.0 License.

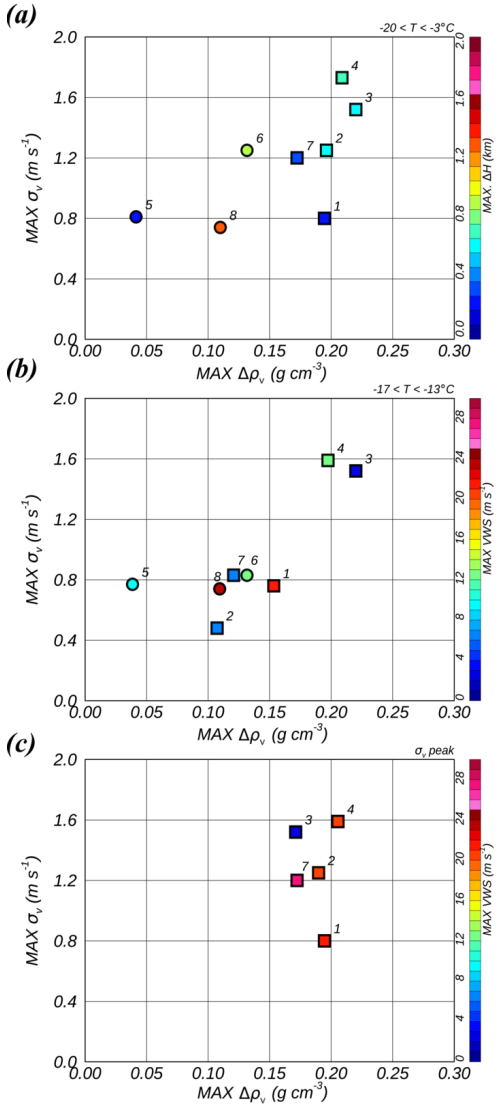


Figure 13. Case-averaged maximum σ_v versus maximum $\Delta\rho_v$. (a) For $-20 < T < -3$°C, colored by the altitude difference between the two maxima. (b) Restricted to $-17 < T < -13$°C, colored by maximum *VWS*. (c) As in (b), but for the σ_v peak zone, colored by maximum *VWS*.

7. Microphysical Evidence: Aggregation Signatures

The preceding sections suggest that the more pronounced σ_v peaks occur where temperature and vapor supply favor planar crystal growth, rather than where atmospheric disturbance is strongest. If that interpretation is reasonable, the polarimetric signature of aggregation would be expected to appear systematically beneath the σ_v peak. Two properties of planar crystals are thought to make aggregation efficient here. The first is geometric. Laboratory investigations show that the aggregation efficiency (E_{agg}) depends strongly on crystal habit: using a large ice cloud chamber, Connolly et al. (2012) reported a

https://doi.org/10.5194/egusphere-2026-6431
Preprint. Discussion started: 9 November 2026
© Author(s) 2026. CC BY 4.0 License.

pronounced peak in E_{agg} near −15°C, with best-estimate values of 0.4–0.9 compared with values generally below 0.2 at other temperatures — a range coinciding with conditions favorable for dendritic growth. The enhancement is attributed to the intricate branch structure of dendrites, which allows crystals to interlock on collision more effectively than simpler geometries, whereas compact particles tend to rebound (Hosler and Hallgren, 1960; Connolly et al., 2012). The second is kinematic: a given mass distributed over a larger projected area raises the collision cross-section, while the broad spread of fall speeds among crystals increases the relative velocity between neighboring particles (Mitchell, 1988; Pruppacher and Klett, 1997). Growth and enhanced aggregation would therefore be expected in vertical succession.

As a first, independent check, hydrometeor class proportions were computed with the winter-precipitation Hydrometeor Classification Algorithm (HCA) of Thompson et al. (2014), a fuzzy-logic scheme whose membership functions were derived specifically for cold-season classes; the classes referred to below are plates (PL), dendrites (DN), ice crystals (IC), and aggregates (AG). The vertical structure of the output is broadly consistent with the expected sequence (Fig. 14): IC dominates the colder levels and the AG proportion increases toward lower levels.

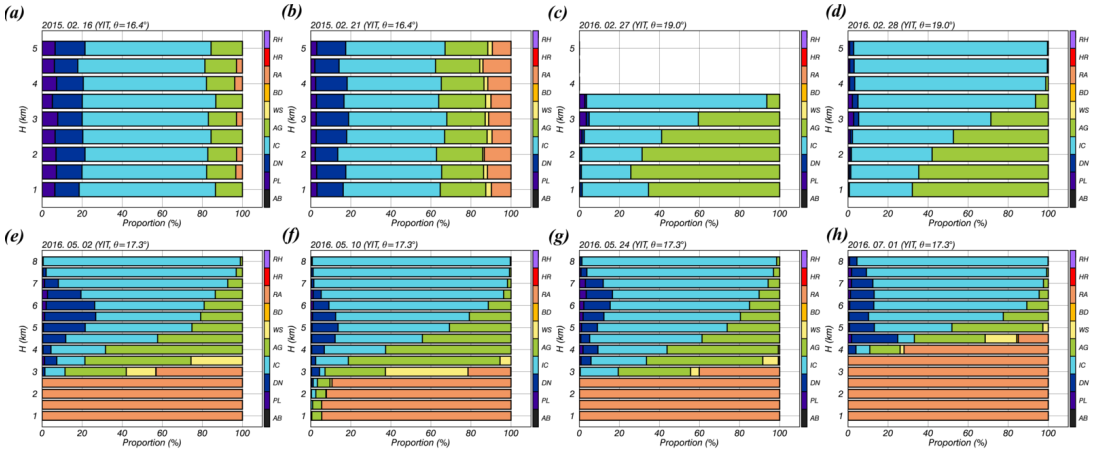


Figure 14. Height-dependent proportions of hydrometeor classes for the eight cases (panels as in Fig. 6), following the winter-precipitation HCA of Thompson et al. (2014); PL, DN, IC, and AG denote plates, dendrites, ice crystals, and aggregates.

Two features of Fig. 14 stand out. In SW3 and SW4 — the cases with the most pronounced σ_v peaks and the largest $\Delta\rho_v$ — the PL and DN proportions are small, yet the AG proportion below the peak is among the largest in the data set. In CP5 and CP6, where no σ_v peak was identified, and in SP7, whose peak lies below the DGZ, the HCA nevertheless indicates appreciable aggregation. The classification therefore registers little dendrite where the σ_v-based evidence is strongest, a pattern that is not consistent with the interpretation developed above and requires explanation. That pattern follows from how the classes are defined. In the above-melting-layer step of Thompson et al. (2014), a gate is assigned DN only where K_{DP} and Z_{DR} are simultaneously elevated — at S band DN is centered on Z_{DR} = 2.6 ± 1.3 dB — whereas AG is centered on Z_{DR} = 0 ± 1 dB, so a gate falls toward AG as Z_{DR} approaches zero. Section 5 established that σ_v and Z_{DR} vary inversely within the DGZ; in exactly the cases where the σ_v peak is most pronounced, the Z_{DR} values therefore lie closest to the AG center rather than the DN center. The low DN and high AG proportions in SW3 and SW4 are in this sense an expected consequence of the classification.

The HCA assigns a hydrometeor type to each gate, that is, it reports the product of the microphysics as a discrete class. The analysis that follows instead seeks the process, expressed as a graded index, and is relatively independent of the HCA: rather than classifying a gate, it examines how the polarimetric variables

https://doi.org/10.5194/egusphere-2026-6431
Preprint. Discussion started: 9 November 2026
© Author(s) 2026. CC BY 4.0 License.

change together with height immediately below the σ_v peak. The approach follows Planat et al. (2021), who identified snowfall microphysical processes from the signs of the vertical gradients of Z_H and Z_{DR}; here K_{DP} is included as a third variable, since within the DGZ its magnitude relates closely to aggregate size and ice particle concentration (Von Terzi et al., 2022).

An aggregation index (I_A) was defined from the co-variability of Z_H, Z_{DR}, and K_{DP}. Each variable was min–max scaled onto [0, 1] using bounds appropriate to ice and snow — 5 to 55 dBZ, −5 to 6 dB, and −1 to 2° km^{-1} — following Kumjian (2013) as adapted by Kumjian et al. (2022); the scaled variables are denoted $\tilde{Z}_H$, $\tilde{Z}_{DR}$, and $\tilde{K}_{DP}$. Scaling places the three on a common numerical footing, without which the sum in Eq. 2 would be dominated by Z_H, and fixes the relative weighting explicitly. The layer beneath the σ_v peak is bounded above by H_σ and below by a level 1 km beneath the σ_v peak zone, or the melting-layer top identified in Fig. 7, whichever is higher. A 1 km standard depth corresponds to the DGZ center-to-bottom distance, spanning −15°C to −8°C under a ~7°C km^{-1} moist-adiabatic lapse rate. Within this layer the slope of each scaled variable was computed with respect to height, the slopes being defined positive in the direction of increase toward the ground. I_A is defined as

$$I_A = \mathrm{s}(\widetilde{Z_H}) - \mathrm{s}(\widetilde{Z_{DR}}) - \mathrm{s}(\widetilde{K_{DP}}) \quad \text{(Eq. 2)}$$

so that I_A is large and positive when Z_H increases toward the ground while Z_{DR} and K_{DP} decrease — the signature expected of aggregation, which increases particle size and sphericity while reducing number concentration (Hobbs et al., 1974; Mitchell, 1988), as reported in polarimetric observations and modeling of snow aggregation (Kumjian and Ryzhkov, 2012). One process shares this signature and must be considered first: riming also increases Z_H while reducing Z_{DR} and K_{DP}, and is not separable from aggregation on gradient signs alone (Moisseev et al., 2017; Planat et al., 2021). Supercooled liquid also occurs in stratiform cloud, so riming cannot be excluded. Aggregation is nevertheless the more consistent explanation here: the signature appears in the lower part of the DGZ, where the aggregation efficiency of dendrites peaks (Connolly et al., 2012), and it strengthens beneath stronger σ_v peaks, as expected if it arises from the planar crystals grown in the peak.

Figure 15 presents this diagnostic in four views. Over the full domain I_A remains near zero for σ_v below about 0.9 m s^{-1} and rises sharply above it (Fig. 15a), a transition driven by SW3 and SW4; against temperature the largest values concentrate in the center of the DGZ, where all four winter cases participate (Fig. 15b). Panels (c) and (d) repeat the comparison for the peak-relative layer, where the threshold behavior becomes cleaner because the moderate values contributed by SW1 and SW2 at fixed temperature fall outside that layer. Dendritic growth depends on temperature and vapor supply together, so a layer selected by a fixed threshold such as −15°C need not coincide with the layer in which growth is most active, and that temperature may differ between cases; defining the layer from the σ_v peak identifies it case by case.

https://doi.org/10.5194/egusphere-2026-6431
Preprint. Discussion started: 9 November 2026
© Author(s) 2026. CC BY 4.0 License.

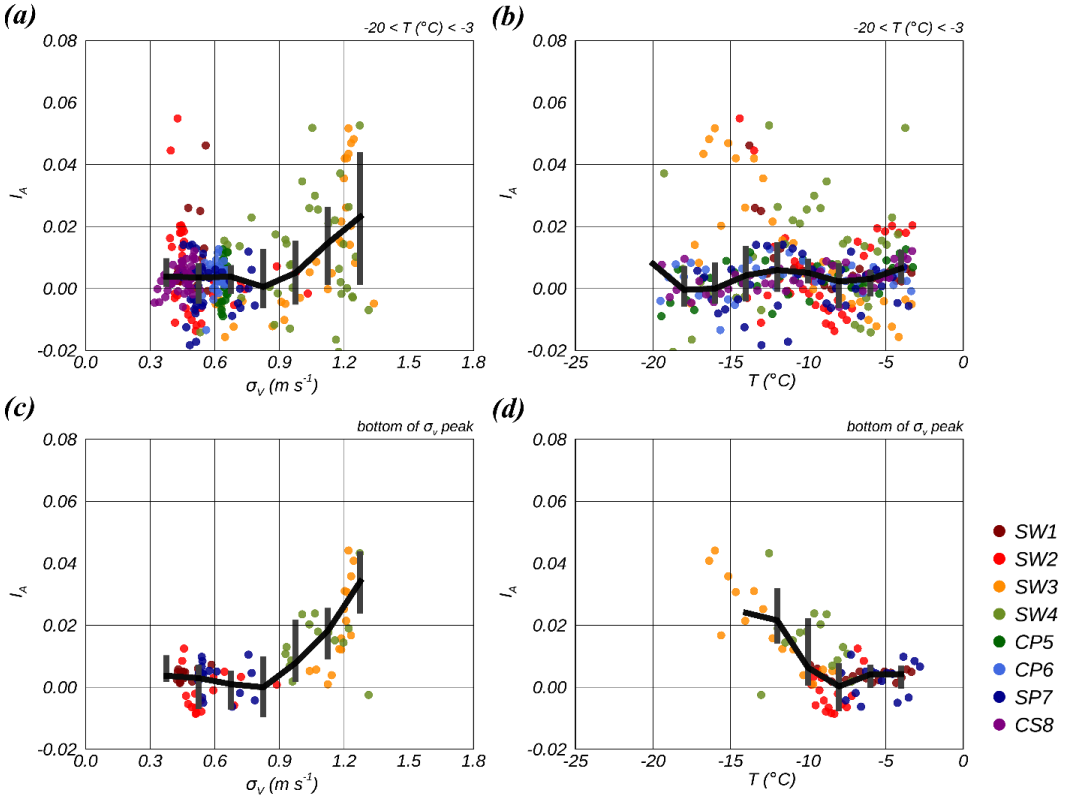


Figure 15. Aggregation index (I_A) versus (a, c) σ_v and (b, d) temperature, for (a–b) the full −20 to −3°C layer and (c–d) the layer immediately below the σ_v peak. Colors denote the eight analysis cases; the black line and error bars show the binned mean ± 1 STD.

A counterpart index was then constructed as a control on I_A. Particle break-up would be the most obvious counter-signature to aggregation, but it produces the mirror image of the aggregation signature, so any index built to detect it would be anti-correlated with I_A by construction and could not test it independently. Vapor-depositional growth was chosen instead because it is a distinct microphysical pathway that leaves a different vertical signature. The resulting growth index (I_G) is specific to plate-like habits, for which depositional growth increases the apparent asphericity and therefore raises Z_{DR}; where growth is isotropic, no systematic change in the sign of Z_{DR} is expected (Kumjian et al., 2022). It is defined as

$$I_G = s(\widetilde{Z_H}) + s(\widetilde{Z_{DR}}) + s(\widetilde{K_{DP}}) \quad \text{(Eq. 3)}$$

so that I_G is large and positive when Z_H, Z_{DR}, and K_{DP} increase together toward the ground, as expected for continued depositional growth of oriented crystals, in contrast to the aggregation signature captured by I_A. I_G shows no comparable relationship with either σ_v or temperature (Fig. 16).

I_G is distributed comparatively uniformly across the domain, with only a weak enhancement below about −15℃, and shows none of the concentration beneath the σ_v peak that characterizes I_A, which supports the aggregation interpretation.

https://doi.org/10.5194/egusphere-2026-6431
Preprint. Discussion started: 9 November 2026
© Author(s) 2026. CC BY 4.0 License.

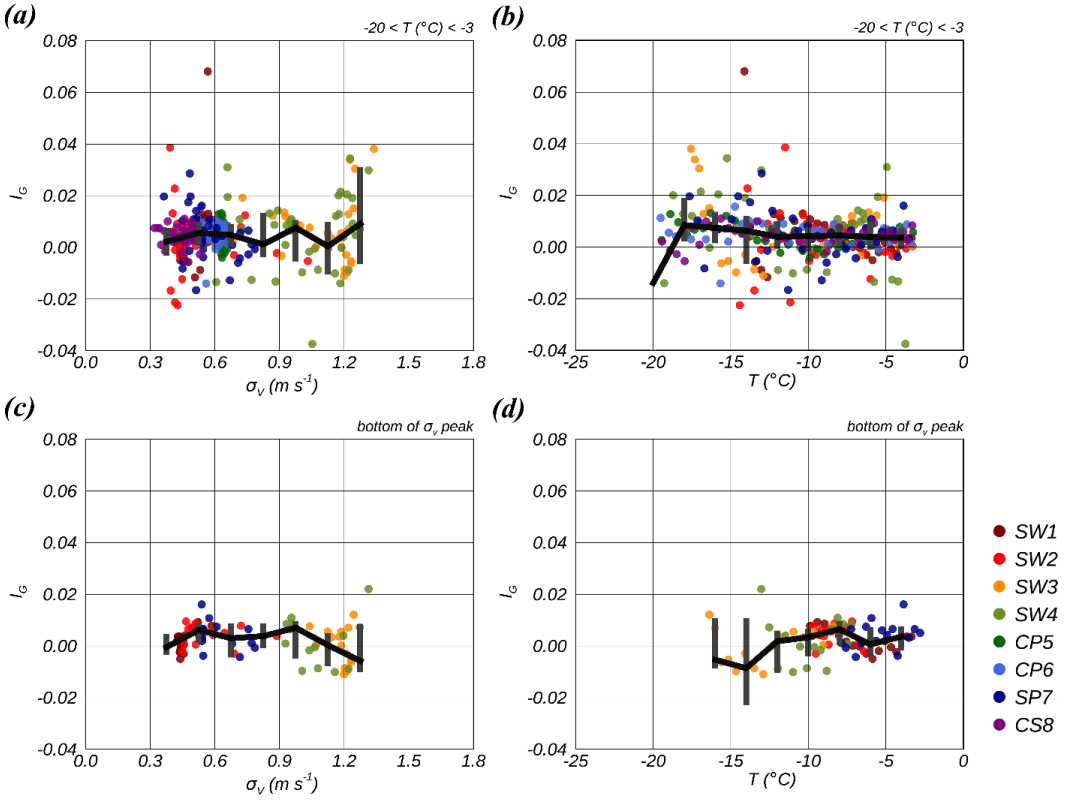


Figure 16. As in Fig. 15, but for the growth index (I_G), which isolates the vapor-depositional-growth signature rather than aggregation.

To make the case-by-case behavior of I_A explicit, the index was averaged within temperature bands divided at −15°C, giving a layer above the growth maximum (−20 to −15°C) and one below it (−15 to −8°C), together with the below-DGZ band (Fig. 17a–c). The layer below the growth maximum behaves similarly to the peak-relative layer, with SW3 and SW4 showing the largest I_A (0.13–0.21) and the remaining cases near zero, but the separation is less distinct and SW3 does not satisfy the full Z_H–Z_{DR}–K_{DP} sign criterion there, whereas under the peak-relative partition both do (square symbols, Fig. 17d).

https://doi.org/10.5194/egusphere-2026-6431
Preprint. Discussion started: 9 November 2026
© Author(s) 2026. CC BY 4.0 License.

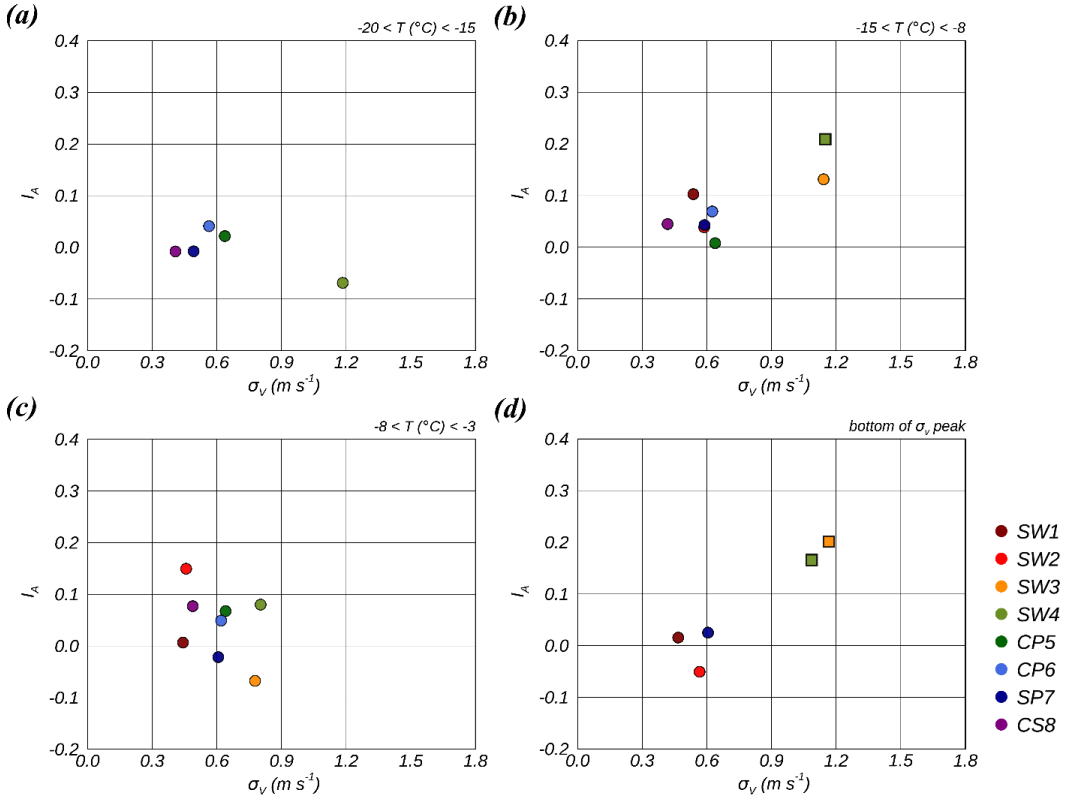


Figure 17. Averaged aggregation index (I_A) versus σ_v, partitioned by temperature: (a) the layer above the −15°C growth maximum (−20 to −15°C), (b) the layer below it (−15 to −8°C), (c) the below-DGZ band (−8 to −3°C), and (d) the layer immediately beneath the σ_v peak. I_A is the sum of the linear-regression slopes of the individually scaled variables with respect to height (Eq. 2). Square symbols denote cases in which Z_H, Z_{DR}, and K_{DP} simultaneously satisfy the aggregation sign criterion.

8. Summary and Conclusion

This study examined whether σ_v peaks observed within the DGZ arise primarily from dynamic forcing — turbulence and wind shear — or from the aerodynamic and microphysical properties of the frozen hydrometeors present in the layer, together with the thermodynamic conditions that produce them.

A spheroidal aerodynamic response model indicated that the external forcing is not the only control on the radial-velocity variance: particle shape matters alongside it, and for spheroidal particles it was shape that exerted the stronger control, with the plane-crystal series responding far more strongly than columnar or rimed habits. Eight cases spanning winter, spring, and summer were analyzed at YIT, and a σ_v peak was resolved in five, all stratiform. In four of these — SW1 to SW4 — σ_v showed no systematic relationship with *VWS* but a temperature-dependent negative relationship with Z_{DR}, suggesting that apparent particle asphericity rather than local shear governs the magnitude of the peak.

The five cases with a resolved peak appear to fall into three regimes. SW3 and SW4 are interpreted as strong dendritic growth: $\Delta\rho_v$ exceeded the 0.2 g m^{-3} threshold, an aggregation signal is present beneath the peak, and near-vertical observations show no updraft signature, all where *VWS* does not appear to be a

https://doi.org/10.5194/egusphere-2026-6431
Preprint. Discussion started: 9 November 2026
© Author(s) 2026. CC BY 4.0 License.

significant contributor. SW1 and SW2 are interpreted as weak growth: their $\Delta\rho_v$ reached values very close to the threshold without exceeding it, so plate-like crystals are the more likely dominant population, consistent with their more modest peaks and the absence of a clear aggregation signal. These two groups differ in degree rather than in kind, both being planar populations. SP7 appears different in kind: its peak lies between about −5 and −10°C, at and below the base of the DGZ rather than within it; it is displaced from the Z_{DR} maximum; no aggregation signal appears beneath it; and although its *VWS* is among the weakest of all cases within the center of the DGZ, within its own peak zone the shear becomes the largest and most variable of any case, the sounding profile reaching about 20 m s^{-1} km^{-1} at the altitude of the peak. SP7 is therefore better regarded as a shear-driven peak unrelated to the DGZ, which suggests the two origins coexist and may be separable only by examining the polarimetric and thermodynamic evidence jointly.

Taken together, the thermodynamic and near-vertical analyses do not support a thermally driven origin: the peak layer was more stable than its surroundings in three of the five cases, and near-vertical V_R showed none of the signature an updraft would produce. The moisture analysis provides the positive association, the maxima of $\Delta\rho_v$ and σ_v being positively related and vertically adjacent across cases, suggesting that the σ_v peak is closely associated with the layer of active planar-crystal growth. Consistent with this, I_A beneath the peak increased with σ_v magnitude while I_G, serving as the control, showed no such relationship — a null result that supports the aggregation interpretation by excluding a generic radar-variable trend.

These results are not intended to identify dendrites as a special target for radar-based turbulence diagnosis. The behavior appears more pronounced for dendrites, but the model results suggest that the property underlying it — a planar geometry whose continuously changing orientation converts a given wind perturbation into a larger radial-velocity variance than compact or rimed particles do — is shared across the plate-to-dendrite series, and that dendrites lie at the extreme of that continuum rather than apart from it. We would therefore suggest that turbulence inferred from σ_v inside a precipitating system be interpreted together with information on the microphysical state and hydrometeor type within that system, and that conditioning CIT and EDR retrievals on hydrometeor type may be worth pursuing. Because this study relies on ground-based observations, direct in-situ verification of hydrometeor habit and fall behavior within the σ_v peak, for example by aircraft probes, remains an important direction for future work.

Appendix. Physical Properties and Simulation Conditions for Frozen Hydrometeors

This appendix summarizes the physical properties assigned to each habit and the conditions under which the Section 2 simulations were performed. Relationships among particle diameter, axis ratio, density, and surface irregularity are listed in Table A1. Habit nomenclature follows the global classification of Kikuchi et al. (2013). Axis ratios for the plane-crystal group follow the hexagonal-crystal formulation of Wang and Denzer (1983), bulk densities follow the micromeritical measurements of Kuroiwa et al. (1967) and the snowflake density measurements of Ishizaka (1993), and crystal-dimension statistics follow Auer and Veal (1970). Terminal fall relationships follow Pruppacher and Klett (2010), with additional constraints from Vázquez-Martín et al. (2021) and ventilation and aggregation considerations from Wang and Kubicek (2013). The equations governing particle motion, drag, sphericity, and the assumed particle size distribution are given in the sections that follow.

Table A1. Summary of the physical properties (diameter D, axis ratio γ, density ρ_s, and the surface irregularity of the snow crystal ε_b) used for the frozen-hydrometeor habits in the Section 2 simulation. Superscript numbers denote the source of each parameter: [1]Kikuchi et al. (2013), [2]Pruppacher and Klett (1997), [3]Nettesheim and Wang (2018), [4]Kuroiwa et al. (1967), [5]Auer and Veal (1970), [6]Vázquez-Martín et al. (2021), [7]Wang and Kubicek (2013), and [8]Rees et al. (2021).

General level	Intermediate level	Elementary level	*D (mm)*	*γ*	*ρ_s (g cm^{-3})*	*ε_b*

https://doi.org/10.5194/egusphere-2026-6431
Preprint. Discussion started: 9 November 2026
© Author(s) 2026. CC BY 4.0 License.

Plane crystal group	Plate	Plate(P1a) 	$0.1 < D < 1.0$ [1]	$\gamma = 0.0398 D^{0.569}$ [3]	0.916 [2]	1.21
	Sector	Sector(P2a) 	$0.5 < D < 2.0$ [1]		0.7572 [4]	1.21
		Board branch(P2b) 			0.3517 [4]	2.61
	Dendrite	Stellar(P3a) 	$1.0 < D < 3.0$ [1]		0.1996 [4]	4.61
		Ordinary dendrite(P3b) 			0.1419 [4]	6.5
Column crystal group	Column	Solid column(C3a) 	$0.1 < L < 0.3$ [1]	$W = 11.3 L^{0.414}$ [5]	$10^{-3} 6.14 L^{0.73} / V$ [6]	1.61
	Needle	Needle(C1a) 	$0.1 < L < 2.0$ [1]	$W = 1.099 L^{0.6108}$ [5]	$10^{-3} 6.64 L^{1.13} / V$ [6]	2.35
Rimed crystal group	Graupel	Lump graupel(R4b) 	$0.1 < D < 3.0$ [1, 7]	$0.95 < \gamma < 1.05$	$10^{-3} (74.25 D^{0.57})$ [8]	1

The irregularity parameter ε_b in Table A1 follows the surface-irregularity correction of Kuroiwa et al. (1967), defined as the ratio of the projected area of a crystal's circumscribing bulk shape to its true projected area. It increases from 1.21 for P1a/P2a to 6.5 for P3b, reflecting the increasing surface complexity from simple plate and sector habits to the highly branched dendrite.

The motion of a particle is governed by $dV_M/dt = (F - F_D)/m$, where V_M is the particle's velocity, m its mass, F the external force acting on it, and F_D the drag force. F_D is expressed as follows:

$$F_D = \frac{1}{2}\rho_g V_M C_D A \quad \text{(Eq. A1)}$$

where ρ_g denotes the atmospheric density and C_D is the drag coefficient of the particle. The expression for C_D optimized for non-spherical particles, proposed by Hölzer and Sommerfeld (2008), is:

$$C_D = \frac{8}{Re}\frac{1}{\sqrt{\Phi_{||}}} + \frac{16}{Re}\frac{1}{\sqrt{\Phi}} + \frac{3}{\sqrt{Re}}\frac{1}{\Phi^{3/4}} + 0.42 \times 10^{0.41(-\log(\Phi))^{0.2}}\frac{1}{\Phi_{\perp}} \quad \text{(Eq. A2)}$$

The three types of sphericity — the sphericity (Φ), the lengthwise sphericity ($\Phi_{||}$), and the crosswise sphericity ($\Phi_{\perp}$) — are defined as:

https://doi.org/10.5194/egusphere-2026-6431
Preprint. Discussion started: 9 November 2026
© Author(s) 2026. CC BY 4.0 License.

$$\Phi = \frac{\pi D^2}{SA} \quad \text{(Eq. A3)}$$

$$\Phi_{||} = \frac{\pi D^2}{4(0.5 \times SA - A_V)} \quad \text{(Eq. A4)}$$

$$\Phi_{\perp} = \frac{\pi D^2}{4A_H} \quad \text{(Eq. A5)}$$

where D is the volume-equivalent particle diameter (mm), S_A is the surface area of the particle (mm^2), and $A_{V(H)}$ is the vertical (horizontal) cross-sectional area of the particle. The basic form of the Reynolds number (Re) is defined as:

$$Re = \frac{\rho_g V_M D}{\mu} \quad \text{(Eq. A6)}$$

where μ represents the kinematic viscosity. The simulations were conducted under the following conditions: the plane-crystal group at 700 hPa and −15°C, the rimed-crystal group at 750 hPa and −10°C, and the column-crystal group at 850 hPa and −5°C. Dendrites have complex effective areas that significantly affect their fall behavior (e.g., Böhm, 1989); accordingly, the aerodynamic properties of four plane-crystal habits were considered separately — sector-like branches (P2a), broad branches (P2b), stellar crystals (P3a), and ordinary dendrite (P3b) — to represent the range of aerodynamic behavior within the plane-crystal group (Table A2).

Table A2. Relationships for C_D–Re and S_A–d for four plane-crystal habits, after Nettesheim and Wang (2018). These relationships are valid for 200 < d (μm) < 5,000.

Types	C_D-Re	SA-d
P2a	$C_D = 23.80 \times R_e^{-0.72} + 0.74$	$SA = 19.44^{-1}(9.50 \times 10^{-1} d^{0.13} - 1.76)^{3.84}$
P2bc	$C_D = 38.85 \times R_e^{-0.87} + 1.09$	$SA = 29.59^{-1}(1.67 \times 10^{-1} d^{0.265} - 0.59)^{3.44}$
P3a	$C_D = 686 \times R_e^{-1.17} + 5.84$	$SA = 160.80^{-1}(1.87 \times 10^{-4} d^{0.89})^{2.27}$
P3b	$C_D = 123 \times R_e^{-0.72} + 0.93$	$SA = 35.05^{-1}(1.94 \times 10^{-3} d^{0.65})^{2.94}$

b. Particle size distribution (PSD) model

The particle size distribution (PSD) follows the exponential form of Sekhon and Srivastava (1970):

$$N(D) = N_0 \exp(-0.1 \Lambda D) \quad \text{(Eq. A7)}$$

To simulate realistic conditions, D in each channel was selected at random. The number concentration [$N(D)$ in mm^{-1} m^{-3}] was calculated for D ranging from 0.5 to 3.0 mm, since most pristine ice-crystal types are observed to have diameters smaller than 3 mm (e.g., Auer and Veal, 1970). The intercept parameter (N_0 in mm^{-1} m^{-3}) and the slope parameter (Λ in cm^{-1}) are given by:

$$N_0 = 2.5 \times 10^3 R^{-0.94} \quad \text{(Eq. A8)}$$

$$\Lambda = 22.9 \times R^{-0.45} \quad \text{(Eq. A9)}$$

where the precipitation intensity (R) was assumed to be approximately 1 mm hr^{-1}, setting the total number concentration (N_T) close to 10^5.

https://doi.org/10.5194/egusphere-2026-6431
Preprint. Discussion started: 9 November 2026
© Author(s) 2026. CC BY 4.0 License.

Author contributions

Dr. Sung–Ho Suh designed the study and collected the samples and performed the study. Dr. Sung–Ho Suh, obtained the results and prepared the manuscript. Dr. Sung–Ho Suh examined the results and checked the manuscript.

Competing interest

None.

Code/Data availability

The data obtained by YIT in this study are available on request from Korea Meteorological Administration (KMA) and the codes are available on request from Dr. Sung-Ho Suh.

Acknowledgments

This research was supported by the NARO Space Center Advancement Project of Ministry of Science and ICT (MSIT) and language editing and proofreading support were provided by Claude during the preparation of this manuscript. The author revised and approved the final text.

References

Allabakash, S., Lim, S., Chandrasekar, V., Min, K. H., Choi, J., and Jang, B.: X-band dual-polarization radar observations of snow growth processes of a severe winter storm: Case of 12 December 2013 in South Korea, J. Atmos. Oceanic Technol., 36, 1217–1235, https://doi.org/10.1175/JTECH-D-18-0076.1, 2019.

Atlas, D., Srivastava, R. C., and Sekhon, R. S.: Doppler radar characteristics of precipitation at vertical incidence, Rev. Geophys. Space Phys., 11, 1–35, https://doi.org/10.1029/RG011i001p00001, 1973.

Auer, A. H., Jr. and Veal, D. L.: The dimension of ice crystals in natural clouds, J. Atmos. Sci., 27, 919–926, https://doi.org/10.1175/1520-0469(1970)027<0919:TDOICI>2.0.CO;2, 1970.

Bailey, M. P. and Hallett, J.: A comprehensive habit diagram for atmospheric ice crystals: Confirmation from the laboratory, AIRS II, and other field studies, J. Atmos. Sci., 66, 2888–2899, https://doi.org/10.1175/2009JAS2883.1, 2009.

Böhm, H. P.: A general equation for the terminal fall speed of solid hydrometeors, J. Atmos. Sci., 46, 2419–2427, https://doi.org/10.1175/1520-0469(1989)046<2419:AGEFTT>2.0.CO;2, 1989.

Chen, H., Xu, W., Liu, N., Sun, J., and Fu, J.: Climatologies of mesoscale convective systems over China observed by spaceborne radars, Mon. Wea. Rev., 150, 2697–2717, https://doi.org/10.1175/MWR-D-22-0002.1, 2022.

https://doi.org/10.5194/egusphere-2026-6431
Preprint. Discussion started: 9 November 2026
© Author(s) 2026. CC BY 4.0 License.

Connolly, P. J., Emersic, C., and Field, P. R.: A laboratory investigation into the aggregation efficiency of small ice crystals, Atmos. Chem. Phys., 12, 2055–2076, https://doi.org/10.5194/acp-12-2055-2012, 2012.

Doviak, R. J. and Zrnić, D. S.: Doppler radar and weather observations, 2nd edn., Academic Press, San Diego, 562 pp., ISBN 978-0-12-221422-6, https://shop.elsevier.com/books/doppler-radar-and-weather-observations/doviak/978-0-12-221422-6, 1993.

Field, S. B., Klaus, M., Moore, M. G., and Nori, F.: Chaotic dynamics of falling disks, Nature, 388, 252–254, https://doi.org/10.1038/40817, 1997.

Gourley, J. J., Tabary, P., and Parent du Chatelet, J.: A fuzzy logic algorithm for the separation of precipitating from nonprecipitating echoes using polarimetric radar observations, J. Atmos. Oceanic Technol., 24, 1439–1451, https://doi.org/10.1175/JTECH2035.1, 2007.

Griffin, E. M., Schuur, T. J., and Ryzhkov, A. V.: A polarimetric analysis of ice microphysical processes in snow, using quasi-vertical profiles, J. Appl. Meteor. Climatol., 57, 31–50, https://doi.org/10.1175/JAMC-D-17-0033.1, 2018.

Hashino, T., Chiruta, M., Polzin, D., Kubicek, A., and Wang, P. K.: Numerical simulation of the flow fields around falling ice crystals with inclined orientation and the hydrodynamic torque, Atmos. Res., 150, 79–96, https://doi.org/10.1016/j.atmosres.2014.07.003, 2014.

Heymsfield, A. J. and Westbrook, C. D.: Advances in the estimation of ice particle fall speeds using laboratory and field measurements, J. Atmos. Sci., 67, 2469–2482, https://doi.org/10.1175/2010JAS3379.1, 2010.

Hobbs, P. V., Chang, S., and Locatelli, J. D.: The dimensions and aggregation of ice crystals in natural clouds, J. Geophys. Res., 79, 2199–2206, https://doi.org/10.1029/JC079i015p02199, 1974.

Hocking, W. K.: Measurement of turbulent energy dissipation rates in the middle atmosphere by radar techniques: A review, Radio Sci., 20, 1403–1422, https://doi.org/10.1029/RS020i006p01403, 1985.

Hosler, C. L. and Hallgren, R. E.: The aggregation of small ice crystals, Discuss. Faraday Soc., 30, 200–207, https://doi.org/10.1039/DF9603000200, 1960.

Hölzer, A. and Sommerfeld, M.: New simple correlation formula for the drag coefficient of non-spherical particles, Powder Technol., 184, 361–365, https://doi.org/10.1016/j.powtec.2007.08.021, 2008.

Ishizaka, M.: An accurate measurement of densities of snowflakes using 3-D microphotographs, Ann. Glaciol., 18, 92–96, https://doi.org/10.1017/S0260305500011319, 1993.

Kennedy, P. C. and Rutledge, S. A.: S-band dual-polarization radar observations of winter storms, J. Appl. Meteor. Climatol., 50, 844–858, https://doi.org/10.1175/2010JAMC2558.1, 2011.

Kikuchi, K., Kameda, T., Higuchi, K., and Yamashita, A.: A global classification of snow crystals, ice crystals, and solid precipitation based on observations from middle latitudes to polar regions, Atmos. Res., 132–133, 460–472, https://doi.org/10.1016/j.atmosres.2013.06.006, 2013.

Kim, J.-H., Park, J.-R., Kim, S.-H., Kim, J., Lee, E., Baek, S., and Lee, G.: A detection of convectively induced turbulence using in situ aircraft and radar spectral width data, Remote Sens., 13, 726, https://doi.org/10.3390/rs13040726, 2021.

https://doi.org/10.5194/egusphere-2026-6431
Preprint. Discussion started: 9 November 2026
© Author(s) 2026. CC BY 4.0 License.

Kumjian, M. R.: Principles and applications of dual-polarization weather radar. Part I: Description of the polarimetric radar variables, J. Operational Meteor., 1, 226–242, https://doi.org/10.15191/nwajom.2013.0119, 2013.

Kumjian, M. R. and Ryzhkov, A. V.: The impact of size sorting on the polarimetric radar variables, J. Atmos. Sci., 69, 2042–2060, https://doi.org/10.1175/JAS-D-11-0125.1, 2012.

Kumjian, M. R., Prat, O. P., Reimel, K. J., van Lier-Walqui, M., and Morrison, H. C.: Dual-polarization radar fingerprints of precipitation physics: A review, Remote Sens., 14, 3706, https://doi.org/10.3390/rs14153706, 2022.

Kuroiwa, D., Mizuno, Y., and Takeuchi, M.: Micromeritical properties of snow, in: Physics of Snow and Ice: Proceedings, Vol. 1, Part 2, Institute of Low Temperature Science, Hokkaido University, Sapporo, 751–772, http://hdl.handle.net/2115/20340, 1967.

Libbrecht, K. G.: The physics of snow crystals, Rep. Prog. Phys., 68, 855–895, https://doi.org/10.1088/0034-4885/68/4/R03, 2005.

Locatelli, J. D. and Hobbs, P. V.: Fall speeds and masses of solid precipitation particles, J. Geophys. Res., 79, 2185–2197, https://doi.org/10.1029/JC079i015p02185, 1974.

Loth, E.: Drag of non-spherical solid particles of regular and irregular shape, Powder Technol., 182, 342–353, https://doi.org/10.1016/j.powtec.2007.06.001, 2008.

Melnikov, V. and Doviak, R. J.: Turbulence and wind shear in layers of large Doppler spectrum width in stratiform precipitation, J. Atmos. Oceanic Technol., 26, 430–443, https://doi.org/10.1175/2008JTECHA1108.1, 2009.

Miloshevich, L. M., Paukkunen, A., Vömel, H., and Oltmans, S. J.: Development and validation of a time-lag correction for Vaisala radiosonde humidity measurements, J. Atmos. Oceanic Technol., 21, 1305–1327, https://doi.org/10.1175/1520-0426(2004)021<1305:DAVOAT>2.0.CO;2, 2004.

Mitchell, D. L.: Evolution of snow-size spectra in cyclonic storms. Part I: Snow growth by vapor deposition and aggregation, J. Atmos. Sci., 45, 3431–3451, https://doi.org/10.1175/1520-0469(1988)045<3431:EOSSSI>2.0.CO;2, 1988.

Moisseev, D., Von Lerber, A., and Tiira, J.: Quantifying the effect of riming on snowfall using ground-based observations, J. Geophys. Res. Atmos., 122, 4019–4037, https://doi.org/10.1002/2016JD026272, 2017.

Moradi, I., Soden, B., Ferraro, R., Arkin, P., and Vömel, H.: Assessing the quality of humidity measurements from global operational radiosonde sensors, J. Geophys. Res. Atmos., 118, 8040–8053, https://doi.org/10.1002/jgrd.50589, 2013.

Muñoz-Esparza, D., Sharman, R. D., and Deierling, W.: Aviation turbulence forecasting at upper levels with machine learning techniques based on regression trees, J. Appl. Meteor. Climatol., 59, 1883–1899, https://doi.org/10.1175/JAMC-D-20-0116.1, 2020.

Nettesheim, J. J. and Wang, P. K.: A numerical study on the aerodynamics of freely falling planar ice crystals, J. Atmos. Sci., 75, 2849–2865, https://doi.org/10.1175/JAS-D-18-0041.1, 2018.

Planat, N., Gehring, J., Vignon, É., and Berne, A.: Identification of snowfall microphysical processes from Eulerian vertical gradients of polarimetric radar variables, Atmos. Meas. Tech., 14, 4543–4564, https://doi.org/10.5194/amt-14-4543-2021, 2021.

https://doi.org/10.5194/egusphere-2026-6431
Preprint. Discussion started: 9 November 2026
© Author(s) 2026. CC BY 4.0 License.

Pruppacher, H. R. and Klett, J. D.: Microphysics of clouds and precipitation, 2nd edn., Kluwer Academic Publishers, 954 pp., https://doi.org/10.1007/978-0-306-48100-0, 1997.

Pruppacher, H. R. and Klett, J. D.: Microstructure of atmospheric clouds and precipitation, in: Microphysics of Clouds and Precipitation, 2nd edn., Springer, 10–73, https://doi.org/10.1007/978-0-306-48100-0, 2010.

Rees, K. N., Singh, D., Pardyjak, E. R., and Garrett, T. J.: Measurement report: Mass and density of individual frozen hydrometeors, Atmos. Chem. Phys., 21, 14235–14250, https://doi.org/10.5194/acp-21-14235-2021, 2021.

Ryzhkov, A. V., Giangrande, S. E., Melnikov, V. M., and Schuur, T. J.: Calibration issues of dual-polarization radar measurements, J. Atmos. Oceanic Technol., 22, 1138–1155, https://doi.org/10.1175/JTECH1772.1, 2005.

Ryzhkov, A., Zhang, P., Reeves, H., Kumjian, M., Tschallener, T., Trömel, S., and Simmer, C.: Quasi-vertical profiles – a new way to look at polarimetric radar data, J. Atmos. Oceanic Technol., 33, 551–562, https://doi.org/10.1175/JTECH-D-15-0020.1, 2016.

Schrom, R. S. and Kumjian, M. R.: Connecting microphysical processes in Colorado winter storms with vertical profiles of radar observations, J. Appl. Meteor. Climatol., 55, 1771–1787, https://doi.org/10.1175/JAMC-D-15-0338.1, 2016.

Sekhon, R. S. and Srivastava, R. C.: Snow size spectra and radar reflectivity, J. Atmos. Sci., 27, 299–307, https://doi.org/10.1175/1520-0469(1970)027<0299:SSSARR>2.0.CO;2, 1970.

Sharman, R. D., Cornman, L. B., Meymaris, G., Pearson, J., and Farrar, T.: Description and derived climatologies of automated in situ eddy-dissipation-rate reports of atmospheric turbulence, J. Appl. Meteor. Climatol., 53, 1416–1432, https://doi.org/10.1175/JAMC-D-13-0329.1, 2014.

Sharman, R. D. and Pearson, J. M.: Prediction of energy dissipation rates for aviation turbulence. Part I: Forecasting nonconvective turbulence, J. Appl. Meteor. Climatol., 56, 317–337, https://doi.org/10.1175/JAMC-D-16-0205.1, 2017.

St-Pierre, M. and Thériault, J. M.: Clarification of the water saturation represented on ice-crystal growth diagrams, J. Atmos. Sci., 72, 2608–2611, https://doi.org/10.1175/JAS-D-14-0357.1, 2015.

Stringham, G. E., Simons, D. B., and Guy, H. P.: The behavior of large particles falling in quiescent liquids, U.S. Geological Survey Professional Paper 562-C, 36 pp., https://doi.org/10.3133/pp562C, 1969.

Suh, S. H., Maki, M., Iguchi, M., Lee, D. I., Yamaji, A., and Momotani, T.: Free-fall experiments of volcanic ash particles using a 2-D video disdrometer, Atmos. Meas. Tech., 12, 5363–5379, https://doi.org/10.5194/amt-12-5363-2019, 2019.

Suh, S. H., Choi, E. H., Kim, H. I., and Jung, W.: Possibility of solid hydrometeor growth zone identification using radar spectrum width, Adv. Atmos. Sci., 40, 317–332, https://doi.org/10.1007/s00376-022-1472-0, 2023.

Thompson, E. J., Rutledge, S. A., Dolan, B., Chandrasekar, V., and Cheong, B. L.: A dual-polarization radar hydrometeor classification algorithm for winter precipitation, J. Atmos. Oceanic Technol., 31, 1457–1481, https://doi.org/10.1175/JTECH-D-13-00119.1, 2014.

Vázquez-Martín, S., Kuhn, T., and Eliasson, S.: Shape dependence of snow crystal fall speed, Atmos. Chem. Phys., 21, 7545–7565, https://doi.org/10.5194/acp-21-7545-2021, 2021.

https://doi.org/10.5194/egusphere-2026-6431
Preprint. Discussion started: 9 November 2026
© Author(s) 2026. CC BY 4.0 License.

Von Terzi, L., Dias Neto, J., Ori, D., Myagkov, A., and Kneifel, S.: Ice microphysical processes in the dendritic growth layer: A statistical analysis combining multi-frequency and polarimetric Doppler cloud radar observations, Atmos. Chem. Phys., 22, 11795–11821, https://doi.org/10.5194/acp-22-11795-2022, 2022.

Wallace, J. M. and Hobbs, P. V.: Atmospheric science: An introductory survey, 2nd edn., Academic Press, Burlington, 483 pp., ISBN 978-0-12-732951-2, https://shop.elsevier.com/books/atmospheric-science/wallace/978-0-12-732951-2, 2006.

Wang, P. K. and Denzer, S.: Mathematical description of the shape of plane hexagonal snow crystals, J. Atmos. Sci., 40, 1024–1028, https://doi.org/10.1175/1520-0469(1983)040<1024:MDOTSO>2.0.CO;2, 1983.

Wang, P. K. and Kubicek, A.: Flow fields of graupel falling in air, Atmos. Res., 124, 158–169, https://doi.org/10.1016/j.atmosres.2013.01.003, 2013.

Williams, C. R.: Vertical air motion retrieved from dual-frequency profiler observations, J. Atmos. Oceanic Technol., 29, 1471–1480, https://doi.org/10.1175/JTECH-D-11-00176.1, 2012.

Williams, E. R., Smalley, D. J., Donovan, M. F., Hallowell, R. G., Hood, K. T., Bennett, B. J., Wolde, M., Bastian, M., and Korolev, A. V.: Validation of NEXRAD radar differential reflectivity in snowstorms with airborne microphysical measurements: Evidence for hexagonal flat plate crystals, 36th Conference on Radar Meteorology, Breckenridge, CO, American Meteorological Society, 15A.6, https://ams.confex.com/ams/36Radar/webprogram/Paper228791.html, 2013.

Willmarth, W. W., Hawk, N. E., and Harvey, R. L.: Steady and unsteady motions and wakes of freely falling disks, Phys. Fluids, 7, 197–208, https://doi.org/10.1063/1.1711133, 1964.

Zhang, P., Chan, P. W., Doviak, R. J., and Fang, M.: Estimate of eddy dissipation rate using spectrum width observed by the Hong Kong TDWR radar, 34th Conference on Radar Meteorology, Williamsburg, VA, American Meteorological Society, P6.9, https://ams.confex.com/ams/34Radar/techprogram/paper_155531.htm, 2009.

Zhang, S., Kumjian, M. R., and Greybush, S. J.: Polarimetric radar-based investigation of microphysics in dendritic and needle temperature aggregation zones during NASA IMPACTS, Mon. Wea. Rev., 153, 2007–2030, https://doi.org/10.1175/MWR-D-24-0232.1, 2025.